**Master's Thesis**

# Comparison of Thin n- and p-type Bulk Silicon Pixel Sensors

# Vergleich dünner n- und p-Typ Silizium-Pixeldetektoren

prepared by

**Julia Rieger**

from Hann. Münden

at the II. Physikalisches Institut

| | |
|---|---|
| **Thesis period:** | 1st April until 30th September 2012 |
| **Supervisor:** | Dr. Jens Weingarten |
| **First Referee:** | PD. Dr. Jörn Große-Knetter |
| **Second Referee:** | Prof. Dr. Arnulf Quadt |
| **Thesis Number:** | II.Physik-UniGö-MSc-2012/08 |

# Contents

# 1. Introduction

In 2013 will be the first long shut-down of the Large Hadron Collider (LHC), the so-called Phase-0 upgrade. During this period of about 20 months, the LHC machine will be prepared for the full design energy and nominal luminosity. The detectors will be consolidated and some upgrades are introduced in order to improve their performances.

The LHC was built as a discovery machine, searching for new physics and improving the precision of the Standard Model of particle physics. Only two month ago, in July 2012, the two multi-purpose detectors, ATLAS and CMS, made a discovery of a neutral boson. This particle is very likely to be the Higgs boson, which was the last undiscovered particle in the Standard Model.
Beside the confirmation, that this new boson is the long-searched Standard Model Higgs particle, there are more tasks on the agenda of particle physicists. The Standard Model does not explain all experimental observations, opening the large area of research of physics beyond Standard Model.
Theories predict production processes of new particles that are rarer than for example the Higgs production. Some extensions of the Standard Model and motivations for searches for physics beyond the Standard Model are described in Chapter 2. To find theses particles an increase of the energy and the luminosity is important.

An important part of high-energy particle detectors is a tracking detector, contributing space points to the track of a particle. Thus, the vertex is determined, enabling b-tagging, and the momentum of a particle can be measured in a magnetic field. The Insertable B-Layer (IBL) will be installed during Phase-0 in order to fulfil the increased requirements.
The number of particles passing the detector increases with the luminosity. By adding a fourth layer to the current ATLAS Pixel Detector very close to the beam pipe, the results of tracking, vertex reconstruction and b-tagging will be more precise. For example, the higher granularity will improve the spatial resolution.
The current ATLAS Pixel Detector is exposed to an integrated fluence of about $1 \cdot 10^{15}$ $n_{\mathrm{eq}}/\mathrm{cm}^2$, whereas the IBL can withstand fluences up to $5 \cdot 10^{15}$ $n_{\mathrm{eq}}/\mathrm{cm}^2$. More details to the ATLAS detector and the upgrades are presented in Chapter 3.

To reach even higher luminosities, the LHC will be upgraded in two further steps. The peak luminosity during LHC Phase-I is expected to be approximately $(2-3) \cdot 10^{34}$ $\mathrm{cm}^{-2}\mathrm{s}^{-1}$. During the Phase-II Upgrade, known as High Luminosity LHC (HL-LHC), the luminosity will increase to at least $5 \cdot 10^{34}$ $\mathrm{cm}^{-2}\mathrm{s}^{-1}$. The innermost detector will have to sustain fluences of more than $2 \cdot 10^{16}$ $n_{\mathrm{eq}}/\mathrm{cm}^2$. Thus, the complete ATLAS inner tracker will be replaced. Due to the high particle flux the sensor material of the detector is required to be radiation hard so it can still be operated after high radiation.

Silicon is the commonly used material for pixel sensors due to its properties and the good availability. A particle passing the sensor creates electron-hole pairs, which induce a signal,

while drifting toward the electrodes in an electric field.

Pure silicon has a large density of intrinsic free charge carriers, preventing the detection of the charge carriers caused by the passing particle. Thus, a combination of n-type and p-type doped silicon is used to produce a usable sensor.

Radiation damage causes defects in the crystal lattice, which change detector properties as is described in Chapter 4. By optimising the design of the sensor, operation even after radiation damage is possible.

The planar pixel sensors of the current ATLAS Pixel Detector have an n-type doped bulk material with a structured grid of $n^+$-type implants. For a short time p-type doped bulk material is available. This n-in-p design potentially has advantages compared to the n-in-n design concerning production costs. In Chapter 5 the differences of these two sensor designs are discussed. In addition, the thickness of the sensor influences the signal height produced by a particle. The electrical field of a thinner sensor is higher compared to a thicker sensor at the same bias voltage.

This research is done with regard to the HL-LHC, which is supposed to be installed in 2022. Hence, new concepts for radiation hard sensors need to be tested, keeping in mind that the planning and building of the ATLAS detector took about 20 years.

During this thesis thin sensors with two different bulk dopings were characterised before and after irradiation. This was done with a laboratory read-out system, which allows performing tests with the samples. The used scans are illustrated in Chapter 6.

Subsequently, in Chapter 7 the results of the four tested samples are presented and the differences are discussed.

# 2. Physics

This chapter introduces the Standard Model of Particle Physics. The elementary particles and their properties are illustrated. Subsequently, limitations of the theory are presented, which evoke extensions of the Standard Model and motivate searches for physics beyond the Standard Model.

## 2.1. Standard Model of Particle Physics

The Standard Model of Particle Physics (SM) [1] reflects our current knowledge of elementary particles and the interactions between them. It successfully describes physical phenomena from scales of about 1 fm and below.
Historically, it has developed from separate theories for electromagnetic, weak and strong force to a unified quantum field theory. The Lagrangian is a function that describes the dynamics and kinematics of a theory. Although it is a unified theory, the Lagrangian is characterised by a $SU(3)_C \times SU(2)_L \times U(1)_Y$ gauge symmetry.
Besides gravity, all fundamental forces are included in the SM, which was finalised in the 1970s. All measurements since then agree with model predictions with high accuracy.

The SM contains 17 particles (and their respective anti-particles) which are divided into fermions and bosons. The latter are particles with an integer spin. Spin-1 bosons are gauge particles that mediate forces. The massless photon ($\gamma$), coupling to electrical charge, is the mediator of the electromagnetic force, the massive $W^{\pm}$ and $Z^0$ are the mediators for the electro-weak interaction, whereas there are eight massless gluons ($g$) that are responsible for the interactions via the strong force.

Fermions are spin-1/2 particles which are subdivided into leptons and quarks arranged in three generations (see Figure 2.1). The mass of these fermions increases with the generation. The higher mass of the particles from the second and third generation explains why they are unstable and have a finite lifetime, while the particles from the first generation are stable and form everyday-matter.
Leptons exit either as charged or uncharged particles that can interact via the weak force. Because the charged leptons carry an electrical charge of -1, they can participate in electromagnetic interactions. Quarks have an electrical charge of $\frac{2}{3}$ or $-\frac{1}{3}$ and they come in three different colours (and anti-colours). This is an additional quantum number and allows interactions via the strong force. Hadronic matter is colourless, hence quarks group to baryons (three-quark state) or mesons (quark-anti-quark state).

In addition, there is a spin-0 boson, the Higgs particle, which is an excitation of the scalar Higgs field. The Higgs mechanism gives mass to the massive gauge bosons. They couple to this scalar field, that breaks the electro-weak symmetry spontaneously (see [3, 4, 5]).
The Higgs particle is the only particle in the SM that is not discovered yet. However, in July 2012 the ATLAS and CMS collaborations made a discovery of a neutral boson with a mass of
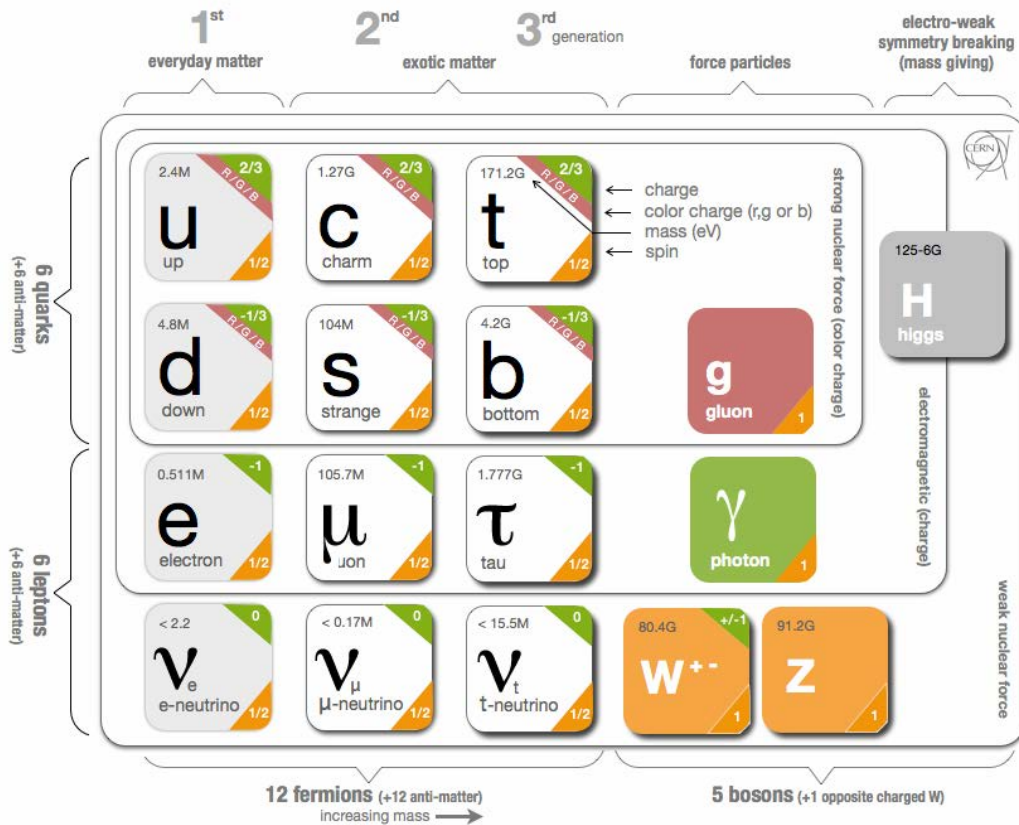
*Figure 2.1.:* Elementary particles in the SM [2].

$126.0 \pm 0.4(\text{stat}) \pm 0.4(\text{sys})$ GeV [6] and $125.3 \pm 0.4(\text{stat}) \pm 0.5(\text{sys})$ GeV [7], respectively. It is compatible with the production and decay of the SM Higgs boson. Further measurements have to prove that this boson is the SM Higgs boson.

## 2.2. Physics Beyond the Standard Model

Despite the success of the SM, there are questions that are not answered yet. There are experimental observations that are not explained by the SM and theoretical problems that imply a lack of understanding. Some of theses problems are illustrated in the following and theories of physics beyond the SM (BSM), which attempt to answer some open questions by introducing new concepts, are mentioned [8].

One of the biggest issues in the SM is that gravity is not included, since general relativity and quantum mechanics are not compatible. In today's particle physics experiments the energy is in a range, that gravitational effects are too small to be detectable. But there is a scale where both quantum and general relativity effects become important, which is known as the Planck scale with $m_P \approx 10^{19}$ GeV. At least at that scale a new theory is needed.
In quantum gravity, it is attempted to develop models that unite quantum mechanics with general relativity to describe quantum phenomena to high energies.

Furthermore, the coupling constants of the electromagnetic, the weak and the strong force are dependent on an energy scale, but they approximately converge at high energy. Grand Unification Theories (GUT) try to extend the SM in a way that the three forces merge into a single interaction characterised by one gauge symmetry and thus unifying the coupling constants.
Theories that predict new particles are an example of unifying the strong with the electro-weak force such as the $W$, $Z$ and Higgs boson were predicted to have a unified electro-weak theory. A theory that could introduce gravity and GUT would be the famed "Theory of Everything".

In addition, astrophysical measurements like rotation curves of galaxies and the cosmic microwave background temperature (see [9]) show that SM matter contributes only about 5% of the universe. The rest is unknown dark energy and dark matter
The best candidate for the latter is a weakly interacting particle with a mass in the 1 TeV-range, which could be introduced by many theories.

Beside the dark energy and dark matter problem, the universe does not contain the predicted amount of anti-matter. During the big bang microscopic processes between particles must have slightly favoured matter over anti-matter. Strong CP-violation could explain the visible matter-anti-matter asymmetry in the universe, but the CP-violation in the SM is not large enough to cause such an asymmetry. Therefore, additional sources of CP-violation in BSM are needed.

Another fundamental problem is the so-called hierarchy problem. The expected Higgs mass, which is in the order of 100 GeV, should receive corrections in the order of the largest scale relevant in the SM like the Planck scale. A solution to this problem can be a fine-tuning. This means that all tree-level and loop contributions to the Higgs mass would compensate in an incredibly precise way, which is often named as unnatural.
But new symmetries and new particles, like in Supersymmetry and Compositeness, could explain the discrepancy as well. In addition, a lower Planck mass, which would introduce changes in the theory of gravity, or extra dimensions, could solve the problem.

There are more problems like the large *number of free parameters* or the large mass range of SM particles. The SM depends on 19 parameters, which are measured in experiments, but the origin of these values is unknown.

Consequently, the SM is an incomplete theory, thus there must be new physics at an energy scale of about 1 TeV. To answer the unanswered questions the Large Hadron Collider was built. It was designed in such a way that it has a large discovery potential and can confirm or disprove many different theories. The unprecedented energy it achieves may even reveal some unexpected results.

# 3. Experimental Setup

## 3.1. Large Hadron Collider

The Large Hadron Collider (LHC) [10] is located at the European Organisation for Nuclear Research (CERN) close to Geneva. It is a proton-proton collider with a design centre-of-mass energy of 14 TeV and thus the highest-energy particle accelerator. There is also a possibility to collide heavy ions. Situated in the former Large Electron-Positron Collider (LEP) tunnel, the LHC is about 100 m below ground and has a circumference of about 27 km.

The particles circulate in two separate beam pipes in opposite directions before colliding. Superconducting magnets providing a magnetic field of about 8.4 T guide the beam particles around the ring. These magnets need to be cooled with superfluid helium to a temperature of 1.9 K to keep the superconducting state.

Within the LHC, the protons are accelerated by 16 radio frequency superconducting cavities with a accelerating gradient of 16 MV/m. Due to this technique no continuous beam is possible, but the protons are grouped to bunches. The design values for the number of protons in one bunch and the number of colliding bunches are $N = 1.15 \cdot 10^{11}$ and $n_{\mathrm{b}} = 2808$, respectively. The bunches are separated by 25 ns, which corresponds to a collision rate of $f = 40$ MHz. In this configuration, the instantaneous luminosity is

$$\mathcal{L} = \frac{n_{\mathrm{b}} N^2 f}{A_{\mathrm{T}}^{\mathrm{eff}}} \sim 10^{34} \ \mathrm{cm}^{-2}\mathrm{s}^{-1},$$

where $A_{\mathrm{T}}^{\mathrm{eff}} = 4\pi\sigma_{\mathrm{b}}^2$ is the effective transverse area of the proton beam with $\sigma_{\mathrm{b}} = 16 \ \mu$m [11]. Together with a total inelastic cross section $\sigma$ of about 60 millibarns (1 barn $= 10^{-24}$ cm$^2$) the collision rate is $\mathcal{L} \times \sigma \sim 10^9$ Hz.

The first collision took place in 2009 with a centre-of-mass energy of 900 GeV, which was increased to 7 TeV for 2010 and 2011. In 2012 the energy has been increased to 8 TeV. Since 2009 a total integrated luminosity of more than 16 fb$^{-1}$ was collected (see Figure 3.1).

The high luminosity of the LHC is needed to produce at least a small number of rare processes like Higgs events and new physics. To capture these events, fast responding, finely segmented and radiation hard detectors are needed.

There are four main experiments where the particles collide. CMS (Compact Muon Solenoid) and ATLAS (A large ToroidaL ApparatuS) are multi-purpose detectors looking for new physics, precision measurements of the SM and the Higgs boson. LHCb (Large Hadron Collider beauty) concentrates on matter-anti matter balance and ALICE (A Large Ion Collider Experiment) on heavy ion collisions.

## 3.2. A Toroidal LHC ApparatuS

With a length of 44 m, a diameter of 25 m and a weight of about 7000 t, the ATLAS detector [13, 14] is the largest detector at the LHC. In the following it is described in more detail.
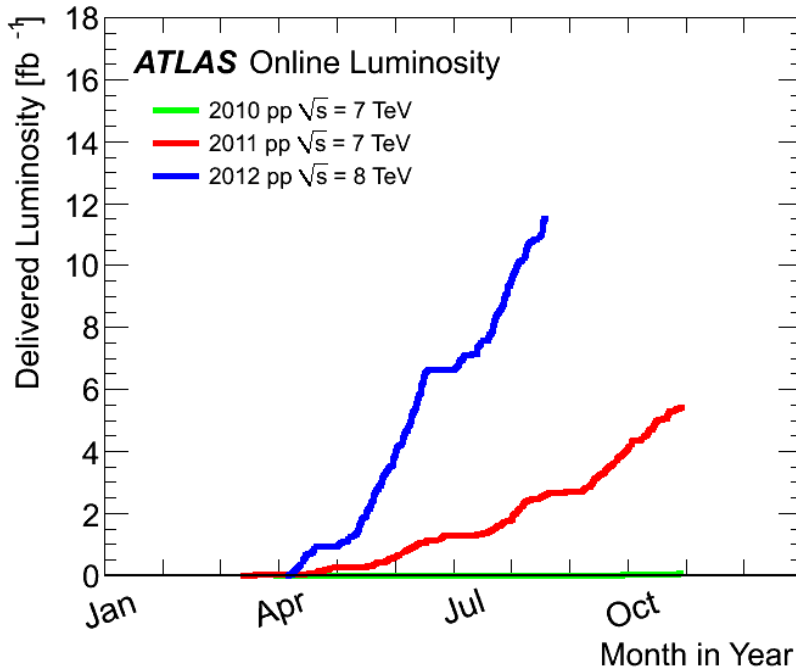
*Figure 3.1.:* Integrated Luminosity versus time for 2010 (green), 2011 (red) and 2012 (blue) (p-p data only) [12].

ATLAS has a forward-backward symmetric cylindrical geometry and consists of a barrel part and end-caps on each side. Not taking into account the small holes for the beam pipe the detector covers a solid angle of $4\pi$. Thus, no detectable particles can escape the detector unseen.

For an explicit geometrical description of the detector, cylindrical coordinates are used. The ATLAS coordinate system is right-handed and has its origin in the centre of the detector. The $z$-axis points in the direction of the beam pipe, the azimuthal angle $\phi$ is measured around the $z$-axis and the pseudorapidity $\eta$ is defined as

$$\eta = -\ln\left[\tan\left(\frac{\theta}{2}\right)\right],$$

where $\theta$ is the polar angle between the particle direction and the $z$-axis.

Considering the collision rate of the proton bunches, about a billion proton-proton events are produced per second. But only the interesting events can be stored. Therefore, the ATLAS Trigger System [15] has to reduce the data rate from 40 MHz to about 200 Hz in three steps.
The first step is the hardware-based Level 1 Trigger (L1), which decreases the rate from 40 MHz to 75 kHz using calorimeter and muon system information. The data is stored in pipeline buffers inside the detector until the L1 decision is made, which takes about 2.5 $\mu$s. From the accepted objects regions of interest (RoI) are built, which are small regions in the $\eta - \phi$ space centred around the object.
The Level 2 Trigger (L2) is a software trigger that restricts itself to the RoI and uses the full resolution and granularity of all detectors in this region. After the decision time of about 10 ms and a reduction of the rate from 75 kHz to about 2 kHz, an event is built.
The last step of the trigger system is the Event Filter (EF), which reduces the rate to about
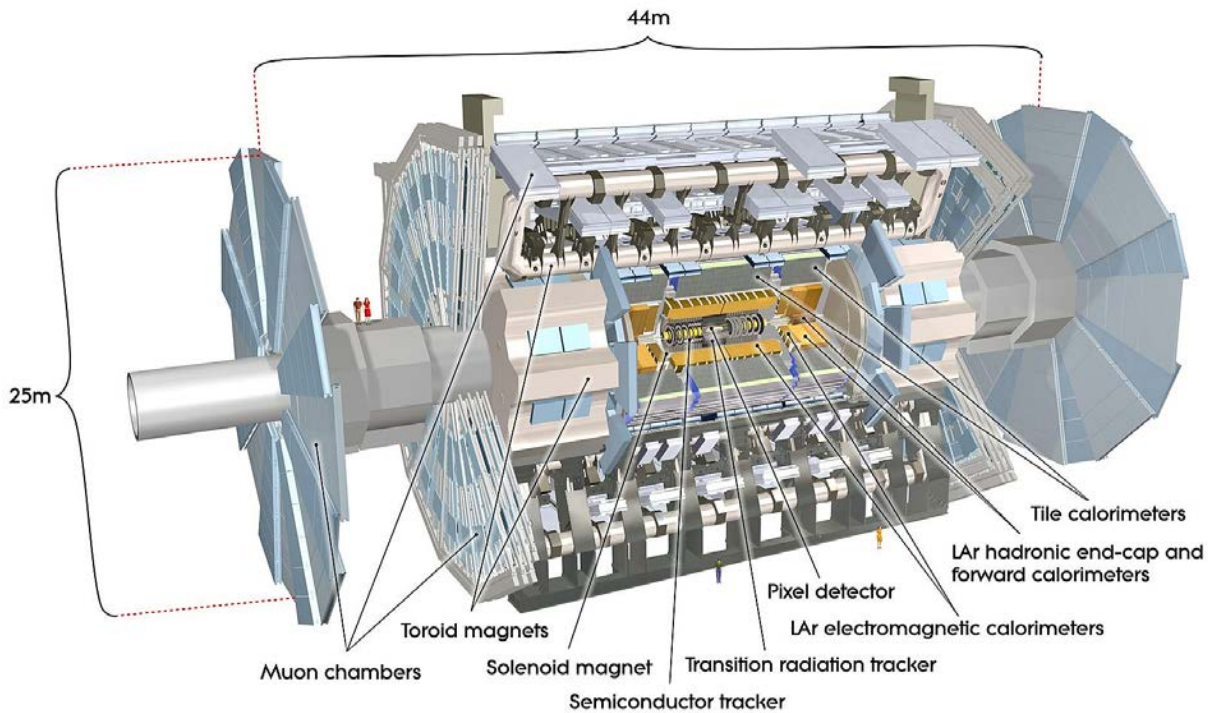
***Figure 3.2.:*** Schematic view of the ATLAS detector [13].

200 Hz. The full event information is accessed and algorithms make the decision in about 4 s. These data sets are then sent to mass storage.

The detector can be divided into several subsystems (see Figure 3.2), in which different particles cause different signatures. The innermost subsystem is a tracking system, which precisely measures the momentum of each charged particle [16]. It is surrounded by a calorimeter system to measure the energy of the particles [17]. The outermost component is a muon detection system [18]. Furthermore, there is the magnet system with a solenoid magnet, which encloses the inner detector, that creates a field of 2 T and a toroid system in the muon system with eight coils that generates a peak field of about 4 T. The fields are used to bend the tracks of charged particles for the momentum measurement.
In the following the subsystems are explained in more detail.

**Muon Spectrometer**   The muon spectrometer is the outermost part of the detector and only muons can normally reach this part. All other known particles, besides neutrinos, are stopped in the calorimeters. The muon system consists of components for triggering and tracking.
Detectors for triggering need to be very fast and to have a good time resolution whereas the spatial resolution is less important. Therefore, precise tracking detectors with a good spatial resolution are needed to measure the bending of the muon track in the magnetic field.
In addition, the special requirements at positions close to the beam pipe have to be taken in account. Due to the higher particle rate at high $\eta$ regions different detectors are needed there.

Thus, there are four different detector types in the muon spectrometer.

For triggering in the central region ($|\eta| < 1.05$) Resistive Plate Chambers (RPC) are used, which are finely segmented gaseous parallel electrode-plates operating in avalanche mode. The Thin Gap Chambers (TGC) in the forward regions ($1.05 < |\eta| < 2.7$) are multi-wire proportional chambers. Both identify charged particles originating in the interaction region.

Drift tubes filled with a gas mixture, which are called Monitored Drift Tubes (MDT), are used in the barrel region ($|\eta| < 2$) for high resolution tracking. In the region $2 < |\eta| < 2.7$ there are Cathode Strip Chambers (CSC), which are multi-wire proportional chambers with strip cathodes.

**Calorimeter System**   The calorimeter system, which is divided into an electromagnetic and a hadronic part, measures the deposited energy of particles by absorbing them. In the ATLAS detector, both parts are sampling calorimeters with active and passive material. The passive material needs to have a high density to form a shower and absorb the particle energy, whereas the active material detects the shower. To measure the total energy of the initial particles, no shower particles are supposed to exit the calorimeters, hence the thickness is about 20 interaction lengths for each type of calorimeter.

The electromagnetic calorimeter, covering the pseudorapidity region $|\eta| < 3.2$, measures the energy of electrons and photons. It has lead absorbers and liquid argon as active material. Liquid argon detectors are radiation hard and can be read out quickly.

All hadrons can be detected by different hadronic calorimeters. The tile calorimeter covering $|\eta| < 1.7$ uses steel as absorber and plastic scintillator tiles as active material. The higher pseudorapidity region $1.5 < |\eta| < 3.2$ is covered by the Hadronic End-cap Calorimeter (HEC). It shares the liquid argon cryostat with the electromagnetic calorimeter, but it uses copper as absorber. Due to its intrinsic radiation tolerance, the liquid argon technology was chosen for the high pseudorapidity regions. Finally, there is the Forward Calorimeter (FCal) for high pseudorapidity regions $3.1 < |\eta| < 4.9$, which uses liquid argon and a dense tungsten matrix.

**Inner Detector**   Stretching over a length of 6.2 m with a diameter of 2.1 m, the Inner Detector (ID) is the innermost component of the ATLAS Detector. At every bunch crossing about 1000 particles emerge from the collision point within $|\eta| < 2.5$ entering the ID. Considering this large track density, fine granularity detectors are needed to achieve the momentum and vertex resolution that is required. Main challenges for the ID are high particle rates and the needed radiation tolerance, which lead to further requirements for read-out electronics and sensor material.

The ID is divided into different sub-detectors, which all need to be reliable, affordable and have as little material as possible in order not to falsify the energy measurement in the calorimeter system.

The outermost part is the Transition Radiation Tracker (TRT), which is composed of about 300,000 straw-tubes embedded in a passive material and filled with a xenon-based gas mixture. On average, a particle crosses 36 straws for $|\eta| < 2.1$ while passing the TRT, which has a spatial resolution of ca 130 $\mu$m. The TRT is not only for tracking, but it can be used for electron identification as well. Electrons passing the passive material emit transition radiation due to the different dielectric constants. This radiation can be detected by the straws.

With four barrel layers and nine endcaps on each side, the Semiconductor Tracker (SCT) is the second tracking detector. It has two layers of single sided p-in-n microstrip sensors that are

rotated against each other by a stereo angle of 40 mrad to get a two-dimensional hit information. The resulting spatial resolution is 16 $\mu$m in $R\phi$-direction and about 580 $\mu$m along the $z$-direction. Finally the innermost component of the ID is the ATLAS Pixel Detector, which is needed for track and vertex reconstruction and b-tagging. It is divided into three barrel-shaped layers and three disks on each side. Due to its position closest to the beam pipe it faces the highest particle flux. The spatial resolution in $R\phi$-direction is 12 $\mu$m and along the $z$-direction about 90 $\mu$m. The main detector components are 1744 sensor-chip-hybrid modules. Each of these modules consists of a 250 $\mu$m thick n$^+$-in-n sensor with 47232 pixels, which are connected to 16 front-end (FE) chips using bump bonding technique. This corresponds in total to approximately $8 \cdot 10^7$ pixels on all modules, most of them have a size of 50 $\mu$m $\times$ 400 $\mu$m, creating a total active area of about 1.7 m$^2$.

## 3.3. ATLAS Pixel Upgrades

2013-2014 will be the first long shutdown of the LHC to prepare the machine for the design centre-of-mass energy of 14 TeV and the nominal luminosity of $10^{34}$ cm$^{-2}$s$^{-1}$. During this period a fourth layer will be inserted into the current Pixel Detector, the so-called Insertable B-Layer (IBL) [19].
With further planned LHC upgrade the luminosity will increase, resulting in more tracks per solid angle. This means a higher fluence and a larger number of hits per pixel necessitating developments of more radiation-hard sensors and faster read-out technology.
When the luminosity is increased by a factor of five, the innermost detector will have to sustain an unprecedented particle fluence of more than $2 \times 10^{16}$ $n_{\mathrm{eq}}$/cm$^2$. Regarding that, the current Pixel Detector is only exposed to a fluence of about $10^{15} n_{\mathrm{eq}}$/cm$^2$, the complete ID has to be replaced. The area of the new tracker will increase by a factor of ten, which calls for more cost-effective sensors.

In the following the focus is on the IBL read-out chip, so-called FE-I4 [20] and the improvements compared to the read-out chip of the current Pixel Detector, FE-I3. The changes in the sensor technology for IBL and future upgrades will be illustrated in Chapter 5.
The FE chip amplifies and digitises the sensor signal in an analogue part and the hit processing is done in the digital part. It is externally supplied with a 40 MHz clock, synchronised with the LHC clock.
The limitations of the FE-I3 [21] concern radiation hardness and high hit rate processing. The FE-I4 shows an increased tolerance to radiation due to the thinner gate oxide transistors which are used. To be able to cope with high hit rates, the digital pixel array was revised. Hits are stored in 4-pixel digital regions until the trigger signal arrives and not in the periphery as before. The transfer of hit information to the chip periphery was the main inefficient part of the FE-I3. By improving the hit processing, the FE-I4 is able to cope with the expected IBL hit occupancy. In addition, the size of the front-end chip is increased. The new pixel array consists of $80 \times 336$ pixels with a size of $50 \times 250$ $\mu$m$^2$, while the current pixel array of $18 \times 160$ had a pixel size of $50 \times 400$ $\mu$m$^2$. Figure 3.3 shows a comparison of both front-ends and the 4-pixel region. It can be seen, that the percentage of the area of the periphery decreased from 25.9% for FE-I3 to 10.6% for FE-I4, which means an increase of the active area of the chip.
Overall, there is a large improvement in the digital part of the readout. The analogue part is still comparable to the current chip and will be described in the following.

The analogue circuit digitises the charge signal that comes from the sensor. Figure 3.4 shows
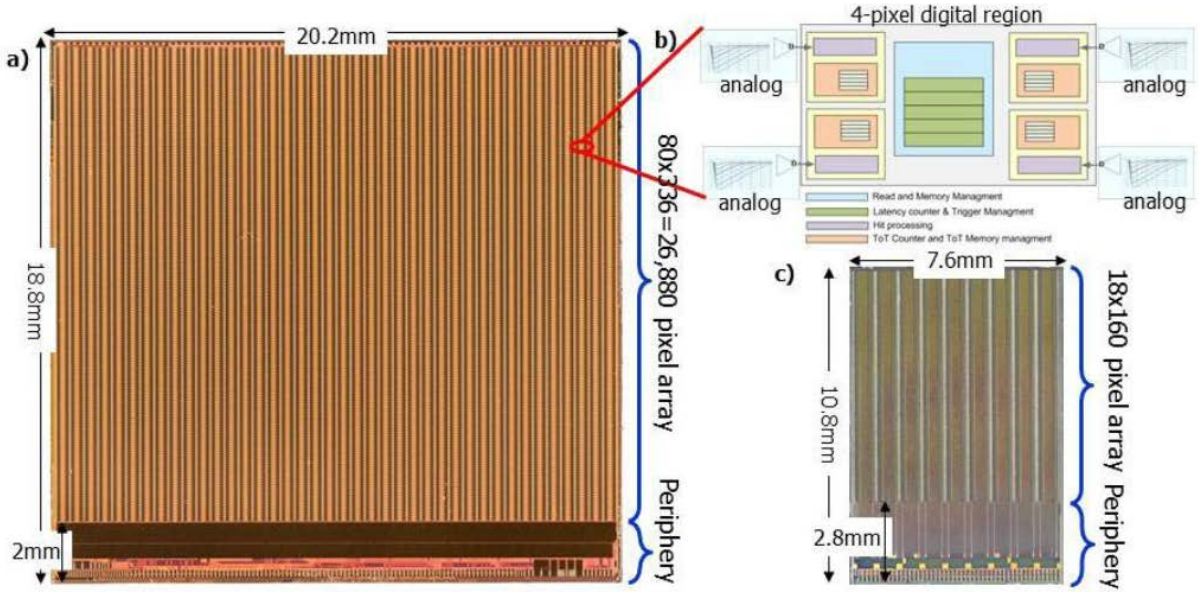
***Figure 3.3.:*** (*a*) Picture of a FE-I4. (*b*) Zoom into a 4-pixel region with separated analogue circuits and a combined digital region. (*c*) Picture of the current FE-I3. [20]

a simplified schematic view of the analogue pixel cell. At first, the signal is amplified in two stages, a fast preamplifier and an AC-coupled second amplifier. The preamplifier integrates the induced charge of the sensor using a feedback capacitor, which is discharged by a constant feedback current. The global feedback current is set by the 8-bit value `PrmpVbpf`, which has a 4-bit in-pixel adjustment called `FDAC`. Its step size is controlled by the 8-bit `FdacVbn`. Thus, the first amplifier forms the signal to a triangular shape (see Figure 3.4), whereas the second stage provides a voltage gain only.

Subsequently, the discriminator compares the input signal with the adjustable threshold. If the signal is higher than the threshold, the output is a logical one and the pixel has a hit, otherwise it is zero. The threshold can be controlled by the temperature compensated value `Vthin_Alt`, which is composed of two 8-bit values for coarse and fine adjustment. Besides the global control, there is a 5-bit in-pixel adjustment named `TDAC`.

In Figure 3.4, the translation from the analogue information of the incoming pulse (amplifier output) into the length of the digital signal (discriminator output) is shown. The time during which there is a logical one is called time-over-threshold (ToT), which is a 4-bit value. The ToT is proportional to the induced charge, because of the constant discharge current. It is measured in clock cycles of 25 ns length, which corresponds to the bunch crossing time.

In order to test a FE chip, there is the possibility of external charge injection. The charge is generated by applying a voltage pulse to different capacitors. The amplitude is controlled by a 10-bit `PlsrDAC` value. Two different capacitors can be selected $C_0$ and $C_1$, which have standard values of about 1.9 fF and 3.9 fF, respectively.
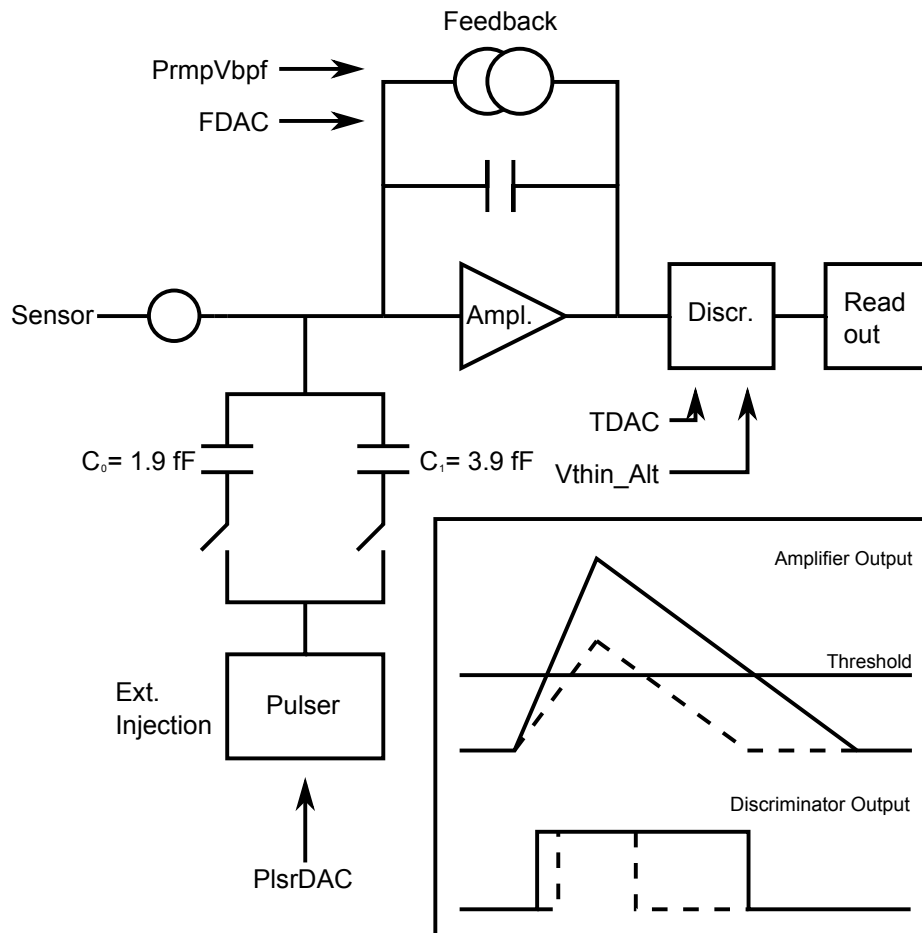
**Figure 3.4.:** Schematic view of the analogue pixel cell. Signals are shaped by a charge amplifier, digitised by a discriminator and then passed on to the digital read-out. Charge can be injected externally via a pulser.

# 4. Principles of Silicon Particle Detectors

Particles moving through matter loose energy. There is energy loss due to ionisation which is caused by interactions with valence electrons and non-ionising energy loss due to scattering off the lattice atoms. Ionisation losses do not lead to any relevant changes in the silicon lattice, because they do not displace atoms.
Damage to the bulk of a silicon sensor limits the lifetime of detectors close to the interaction point. It is caused mainly by displacement of lattice atoms in elastic scattering forming defect centres.

Before looking at particular sensor designs for IBL and future silicon pixel detectors, the working principles of these detectors as well as implications of radiation damage are illustrated. The latter is especially important keeping in mind the position of the detector close to the beam pipe and the number of particles passing through the sensor.

## 4.1. Fundamental Properties of Silicon

Most high-resolution particle tracking detectors in high energy physics are made out of silicon, which is a crystalline solid-state semiconductor. To understand why this is an adequate material, a closer look to semiconductor physics is needed [22].

In the energy-band theory, a material is described by introducing a valence band and a conduction band. Valence electrons are bound to individual atoms, whereas electrons in the conduction band can move freely in the atomic lattice.
In metal, these two bands overlap, which explains the good conductivity, whereas an insulator has in between a large band gap, usually larger than 3 eV. The band gap of a semiconductor is usually smaller than 3 eV thus atoms can be ionised with a small amount of energy leading to mobile ("free") charge carriers in the sensor.
There are two different types of band gaps in semiconductor physics, a direct band gap or an indirect band gap. In a semiconductor with a direct band gap, the momentum of the electrons and holes is the same in the conduction band and the valence band. In contrast, a band gap is called indirect if the electron has to change its momentum in order to get from the valence to the conduction band. Silicon is an indirect semiconductor, so the average energy required to lift an electron to the conduction band is $I_0 = 3.62$ eV [22]. This is about 10 times smaller than the energy required for gas ionisation.

The advantage of silicon in contrast to other semiconductors is the good availability and a small band gap. Silicon is produced by many industrial firms in a very good quality. Due to the crystalline structure, silicon has the disadvantage that it is sensitive to radiation damage.

The basic operating principle of semiconductor detectors is the creation of electron-hole pairs due to the passage of ionising radiation. The charge carriers induce a signal, while drifting toward the electrodes due to an electric field.

## 4.2. Energy Loss of Particles

Different particles behave differently while passing through matter. Depending on properties of the particles such as charge, mass and energy, various processes determine their signatures in matter. These mechanisms are shown in the following [22, 23].

If a charged particle with a mass well above the electron mass ($M \gg m_e$) penetrates the material, the main process of losing energy is ionisation, where electron-hole pairs are produced. These free charge carriers can be extracted by an externally applied electrical field. The amount of energy lost per distance is described by the Bethe-Bloch formula

$$-\langle\frac{\mathrm{d}E}{\mathrm{d}x}\rangle = 2\pi N_A r_e^2 m_e c^2 \rho \frac{Z}{A} \frac{z^2}{\beta^2} \left\{ \ln\left(\frac{2m_e c^2 \beta^2 \gamma^2 W_{\max}}{I^2}\right) - 2\beta^2 - \delta - 2\frac{C}{Z} \right\},$$

where $r_e$ is the classical electron radius, $m_e$ the electron mass, $N_A$ Avogadro's number, $I$ the mean excitation potential, $Z$ the atomic number of the absorbing material, $A$ atomic weight of absorbing material, $\rho$ the density of the absorbing material, $z$ the charge of an incident particle in units of $e$, $\delta$ the density correction, $C$ the shell correction and finally the maximum energy transfer $W_{\max}$ in a single collision.

The formula has a minimum at $\beta\gamma = 3.5$ which corresponds to an energy loss of $\langle\frac{\mathrm{d}E}{\mathrm{d}x}\rangle \approx 1.5\frac{\mathrm{MeV\ cm}^2}{\mathrm{g}}$ (see Figure 4.1). Particles with a momentum causing this energy loss are called
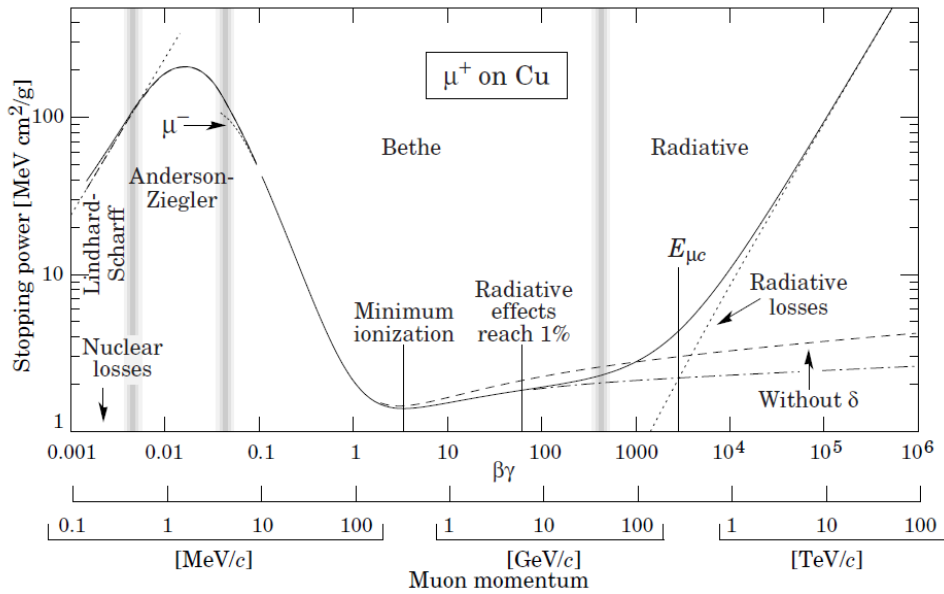


***Figure 4.1.:*** Stopping power ($= -\langle\frac{\mathrm{d}E}{\mathrm{d}x}\rangle$) for positive muons in copper as a function of $\beta\gamma = p/Mc$ [24].

minimum ionising particles (MIP).

The total energy loss of electrons is composed of two components. Next to the energy loss described by the Bethe-Bloch formula, electrons can loose their energy by bremsstrahlung. This

is electromagnetic radiation which is emitted if an electron is scattered in the electrical field of a nucleus. Due to the acceleration the radiation is emitted, which is the dominating mechanism of energy loss at high energies. In addition, the Bethe-Bloch formula has to be modified due to the small mass of electrons.

The behaviour of photons in matter is completely different from the mechanisms described above for charged particles. Because they are not charged, there are no inelastic collisions with electrons. The three most important processes are the photoelectric effect, Compton scattering and pair production.
The cross section of these processes depends on the photon energy and the material. If the photon energy is between the $\mathcal{O}(\text{eV})$ and $\mathcal{O}(100 \text{ keV})$, the photoelectric effect is the most probable process. An electron is emitted by absorbing a photon, whose energy has to be larger than the binding energy of the electron. The rest of the photon energy contributes to the kinetic energy of the electron.
At photon energies between $\mathcal{O}(100 \text{ keV})$ and $\mathcal{O}(10 \text{ MeV})$ the Compton effect is dominating. The photon scatters on a quasi-free electron and transfers a part of its energy to the electron.
For high energy photons, pair production is the most important process. With a photon energy, which is higher than twice the electron mass ($\mathcal{O}(\text{MeV})$), an electron-positron pair can be produced.

Due to these reactions photons have a much larger penetration depth and a beam of photons attenuated, while passing through matter. The intensity of a beam decreases exponentially with the thickness of the passed material $x$ [23]

$$I(x) = I_0 e^{-\mu x},$$

with the initial intensity $I_0$ and $\mu$ the material-specific and energy-dependent mass attenuation coefficient.

Massive neutral particles, like neutrons, cannot interact via the electromagnetic force. Instead, they take part in elastic scattering processes and nuclear reactions.

## 4.3. p-n Semiconductor Junction

Knowing the density $\rho$ and the average energy for electron-hole creation $I_0$ of silicon, the signal charge $Q$ of a MIP can be calculated as

$$Q = \frac{\langle \frac{\text{d}E}{\text{d}x} \rangle \rho d}{I_0}.$$

Assuming a sensor with a thickness of $d = 250 \ \mu\text{m}$ the average generated charge is $Q = 24000 \ e$. The current induced by the electron-hole pairs created by a MIP is much smaller than the one induced by thermal charge carriers. At room temperature ($T = 300$ K) the density of intrinsic free charge carriers is $1.02 \cdot 10^{10} \text{ cm}^{-3}$ [25]. In a pixel with a size of 50 $\mu$m $\times$ 400 $\mu$m there are about $5 \cdot 10^7$ free electrons. Thus, pure silicon is not suitable as sensor material.

In order to modulate its electrical properties, a semiconductor can be doped. Doping intentionally introduces impurities into the material. A donor atom introduces states close to the conduction band. Electrons in these states can be easily excited, becoming free electrons. In

contrast acceptor atoms provide holes, which are unoccupied states in the valence band. Thus, the impurities act as donors or acceptors.

Semiconductors doped with donor impurities are called n-type, while those doped with acceptor impurities are known as p-type. The names indicate the type of the majority charge carriers.

A combination of n-type and p-type silicon is used to produce a sensor with very low leakage current and low free charge carrier concentration. At the emerging p-n-junction the majority charge carriers recombine until there is a stable configuration in the crystal. Typical doping concentrations are in the range between $10^{13}$ cm$^{-3}$ and $10^{18}$ cm$^{-3}$, whereas the density of intrinsic free charge carriers is as already mentioned $1.02 \cdot 10^{10}$ cm$^{-3}$. Hence, in contrast to pure silicon, in doped silicon, the additional electrons and holes become the most important charge carriers.

In the formed depletion zone, the immobile positively charged donor atoms remain in the n-type and the negatively charged acceptor atoms in the p-type silicon, which are also called space charges [26] (see Figure 4.2). The width of the depletion zone can be increased by applying a
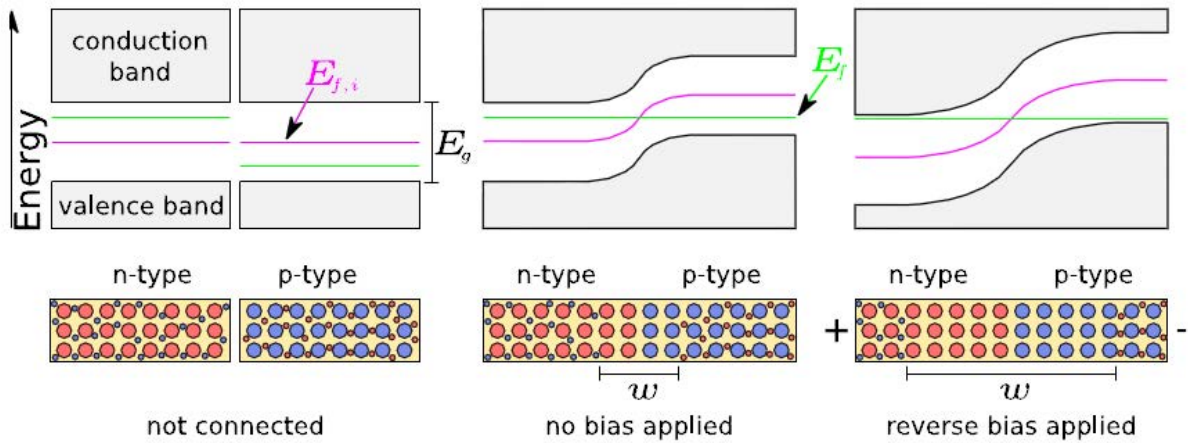


***Figure 4.2.:*** Working principle of a p-n-junction. $E_\text{f}$ is the Fermi energy of the doped material in contrast to the intrinsic value $E_\text{f,i}$. The width $w$ of the depletion zone increases when a bias voltage is applied. The diode formed by the p-n-junction is reverse biased [26].

bias voltage and it is influenced by the concentration of donors and acceptors and the temperature.

Ideally, there should be no free charge carriers in the sensor, meaning the width of the depletion zone should be equal to the width of the sensor. The bias voltage needed to achieve this state is referred to as depletion voltage. Hence, ideally there is only a current if a particle penetrates the sensor producing electron-hole pairs. But because of the thermal generation rate of charge carriers, there is always a small leakage current.

Material properties like the effective doping concentration influence the depletion voltage (see Section 4.4). If the bias voltage is too high a junction break-down can happen. It is characterised by a huge increase of the leakage current. There are three possible sources for a break-down: thermal instability, tunnelling and avalanche multiplication.

Thermal instability can happen when the sensor heats up caused by a large power dissipation.

The thermal generation rate of free charge carriers increases with temperature, leading to increased leakage current. This leads to a positive feedback which results in thermal runaway of the leakage current.

Secondly, at high bias voltages the band structure is more deformed until band-to-band tunnelling of charge carriers is strongly increased. Finally, at very high electrical fields the free charge carriers are strongly accelerated so that they can create more charge carriers by impact ionisation. This can lead to an avalanche.

## 4.4. Implications of Defects

If the energy transferred from a particle to a silicon atom is larger than about 25 eV [27] a defect is caused. There are point defects like vacancies, which are missing atoms in the lattice, interstitials, which are extra silicon atoms, and substitutionals, meaning a impurity atom on a silicon lattice site. Furthermore, there can be more complex defects like cluster defects. Figure 4.3 shows a schematic view of some possible defects.
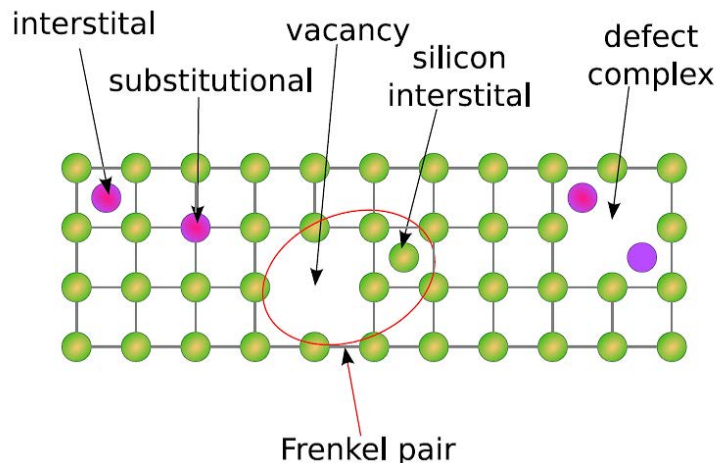


***Figure 4.3.:*** Possible defects that can occur in a crystal lattice [26].

These defects change the properties of the silicon are changed, which leads to additional localised states in the bandgap. These energy levels then act as donors or acceptors and change the effective doping. The main effects on detector properties due to bulk defects are an increase of the leakage current, a reduction of the signal height and a change in the effective doping concentration. The latter effect leads to a change in the depletion voltage. In the following, the reasons for these detector effects are summarised [28]. Figure 4.4 illustrates five main effects, namely generation, recombination, trapping, compensation and tunnelling. There will be three further effects explained that do not have an easy graphical illustration.

A defect which is in the middle between valance band and conduction band can increase the thermal generation rate. The defect acts as a rest stop which divides the band gap in two smaller energy steps. A bound electron is thermally excited to the defect centre and then excited to the conduction band. A free electron-hole pair is created, which causes an increase of the leakage
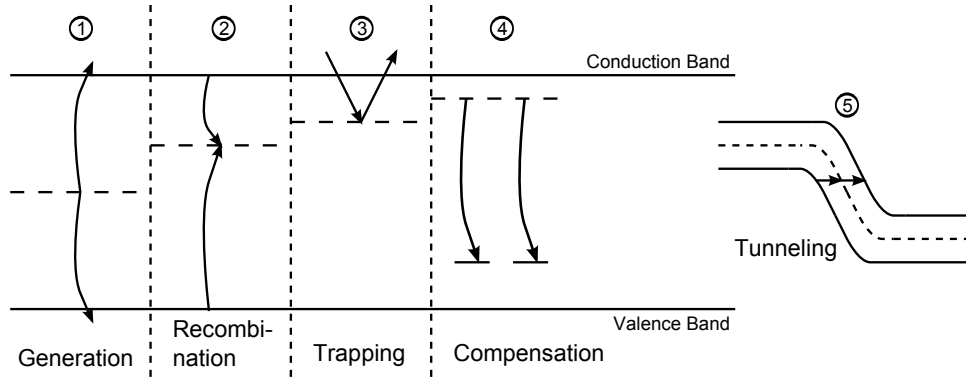
**Figure 4.4.:** Schematic illustration of five main implications of defects in silicon.

current.

Recombination of electron-hole pairs is a well known process which decreases the signal size. There are defect centres that can capture charge carriers of opposite sign and consequently increase the recombination rate. The life time of a charge carrier decreases as well as the signal size.

Moreover, defect centres can temporarily trap charge carriers at a typically shallow level. Later they are emitted again. If the trapping time is longer than the read-out time of the sensor, this leads to a reduced signal height. This effect is expected to be the dominant effect for reduced charge collection efficiencies at the HL-LHC [26].

The compensation of donors or acceptors by radiation-induced centres is an effect resulting in a changing doping concentration. It is more probable to compensate donor states than acceptor states. For example, in n-type material free electrons are compensated by radiation-induced acceptors. The result is a reduced concentration of negative charge carriers.

A process which is supported by defect centres is the tunnelling of charge carriers through a potential barrier from the valence to the conduction band (see Figure 4.4). This is another effect that increases the device current.

Radiation induced defects can act as scattering centres which reduce the mobility of the charge carriers. As a consequence, the drift velocity and the induced current decrease and again a smaller signal is measured.

The removal of charge carriers can lead to a type inversion, which is as well called space charge sign inversion. The effective doping concentration changes from positive to negative, converting an n-type doped material into a material, which has acceptor-like states similar to a p-type material.
For the present ATLAS n-in-n pixel sensors a type inversion has been measured in lab conditions [29]. Figure 4.5 shows the absolute effective doping concentration and the depletion voltage as function of the fluence. Starting with an n-type bulk material, a decrease of the effective doping concentration can be seen. After the donor removal acceptor-like states dominate.
The increase of the acceptor concentration $N_A$ leads to an increase of the depletion voltage $U_{depl}$
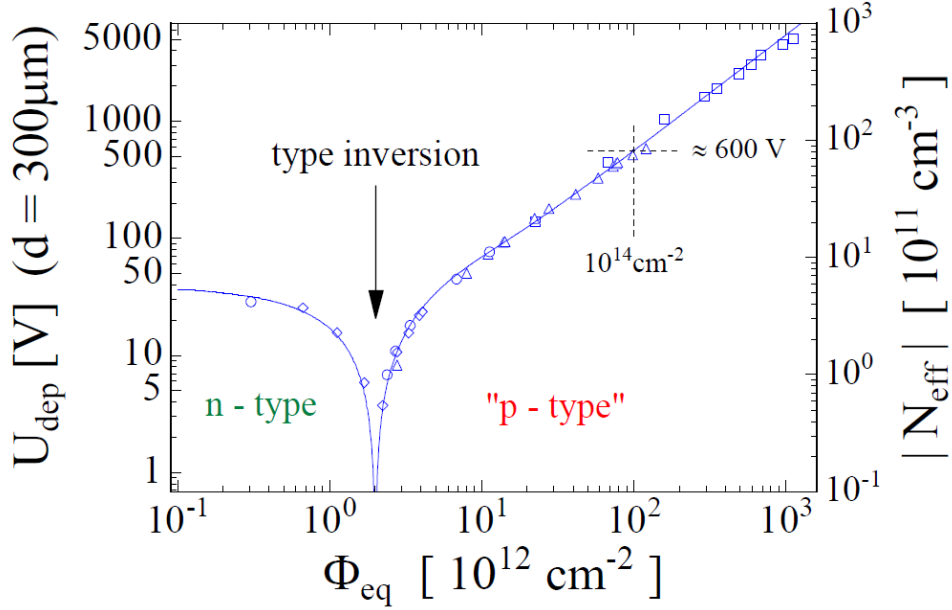
***Figure 4.5.:*** Absolute effective doping concentration in dependence of the fluence, which is shown in damage equivalent to 1 MeV neutrons [29].

which depends on effective doping concentration $N_{\text{eff}}$ as [22]

$$U_{\text{depl}} = \frac{|N_{\text{eff}}|q}{2\epsilon\epsilon_0}d^2$$

with

$$N_{\text{eff}} = N_{\text{D}} - N_{\text{A}}.$$

$N_{\text{D}}$ is the donor concentration. The width of the space-charge region $d$ is equal to the thickness $D$ of the sensor at a voltage of $U_{\text{depl}}$.

At a certain effective doping concentration, the sensor has to be operated partly depleted, if the maximum applicable bias voltage, set by the used cables and power supplies, is reached. This leads to a decrease of the signal.

Furthermore, the effectiveness for thermal generation of carriers is enhanced when defects are located in a region with a high electric field. A possible explanation could be the Poole-Frenkel effect, a reduced potential barrier for thermal generation (see [30]), and it is another source for a higher leakage current.

In summary, the presence of defects caused by radiation leads to higher leakage currents and a reduced signal. An increase of the noise is one result of a larger leakage current. Together with a smaller signal, the signal to noise ratio decreases significantly. In addition more powerful cooling systems are needed to compensate the larger power dissipation due to the higher leakage current. The cooling systems increase the inactive material in the detector.

In order to model the radiation damage of material, the Non-Ionising Energy Loss (NIEL) hypothesis is a useful tool [31]. It aims to scale the radiation damage of different particles and

due to different energies. The basic assumption of the hypothesis is that any induced change displacement-damage $D(E)$ in the material scales linearly with the amount of energy deposited in the material as

$$D(E) = \frac{A}{N_A} \left. \frac{\mathrm{d}E}{\mathrm{d}x}(E) \right|_{\text{non-ionising}}$$

$E$ is the energy of the incident particle, $\mathrm{d}E/\mathrm{d}x$ the specific energy loss, $A$ is the atomic weight of the target material and $N_A$ is Avogadro's constant.

There are small discrepancies between the model predictions and measured damage, which could be caused by some assumption of the hypothesis. But the differences could be explained as well by experimental uncertainty of environment variables during the radiation, like the homogeneity of the beam or temperature fluctuations.

All in all the NIEL hypothesis works very well to scale the radiation damage of any particle to the damage of 1 MeV neutrons.

## 4.5. Defect Annealing

Not all defects generated by radiation are stationary or permanent. The mobility of defects depends on the temperature. Even at room temperature some defects are mobile. Moving defects can form new complex defects or they can recombine and recover the damage.

Figure 4.6 shows the annealing behaviour of the radiation-induced change in the effective doping concentration $N_{\text{eff}}$ at a temperature of 60°C. The change of the effective doping concentration
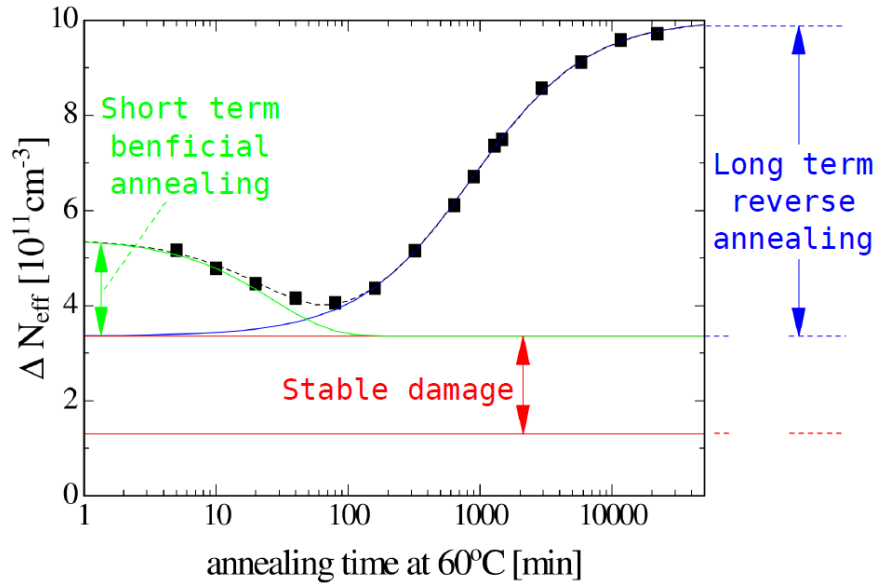


***Figure 4.6.:*** Change of the effective doping concentration as a function of annealing time at a temperature of 60°C showing short-term, long-term annealing and stable damage [26].

$N_{\text{eff}}$ is composed of three different components: short-term beneficial annealing, stable damage and long-term reverse annealing [31].

Short-term and long-term annealing depend on the annealing temperature corresponding to the annealing time and the fluence. Beneficial annealing refers to a decrease of the change of the

effective doping concentration towards the stating configuration, which takes place in the first hour. In contrast, reverse annealing amplifies the change of the effective doping concentration, happening at a longer time scale. Stable damage is not depending on annealing but only on the fluence.

With carefully chosen annealing parameters a controlled beneficial annealing of some bulk defects is possible. For example, irradiated sensors need to be stored and operated at low temperatures in order not to change the situation after irradiation.

# 5. Designs of Silicon Pixel Sensors

In order to get a precise momentum and vertex measurement, a fine segmentation of the read-out electrodes is required. Widely used is a segmentation into strips, which are rectangular-shaped electrodes with a length basically as long as the sensor and a width on the order of 10 $\mu$m. Two layers of strip detectors, rotated with respect to each other, are needed to get a two-dimensional hit information.

Pixels, meaning electrodes with edges of similar length, provide an easier determination of the two-dimensional information with only one layer. Each pixel cell is realised by a pixelated implant on a doped bulk material. The doping type of the implant and the bulk material gives the name to the sensor design, such as p-in-n, n-in-n or n-in-p sensors.

P-in-n sensors are successfully used in all pixel applications which do not require radiation hardness as explained later. The current ATLAS Pixel Detector uses the same bulk doping, but n-type pixels in order to improve the radiation hardness. Only for a short time sensors with a p-type bulk are available in a useable quality, so that n-in-p sensors are candidates for future detectors. These planar pixel sensors are the common technology in high-energy particle physics.

The design of a sensor can be optimised in order to improve operation after radiation damage. In this context, n-in-n and n-in-p designs are discussed in the following as well as the behaviour and advantages of thin planar sensors.

## 5.1. n-in-n Design

A planar n-in-n sensor consists of a lowly n-doped substrate, which contains $n^+$ implantation on the front side and one large $p^+$ implantation on the back side. In this context $n^+$ and $p^+$ pixels have a high doping concentration. The negative bias voltage is connected to the p-doped electrode, which is surrounded by a multi-guard ring structure.

The purpose of the guard rings is a controlled voltage drop from the high voltage pad to the edges of the sensor. Thus they protect the front-end chip from discharges. Otherwise, the back side potential would be forwarded to the side facing the front-end chip via the conductive cutting edges. To implement the guard ring structure double-sided processing is necessary, which is difficult and thus expensive.

The n-in-n design has advantages compared to p-in-n sensor technologies concerning radiation-induced type inversion (see Section 4.4), because it can be operated partly depleted. To explain this advantage a closer look is taken at the formation of the depleted region in the sensor.

For unirradiated sensors, the depletion zone starts at the back (p) side and the pixels are not isolated from each other until full depletion (see Figure 5.1). After type inversion the depleted region propagates from the $n^+$-pixel side towards the $p^+$ implantation. The pixels are insulated even if the sensor is not fully depleted. This is especially important when the maximum bias voltage is reached, keeping in mind, that the depletion voltage increases with increasing fluence (see Figure 4.5).
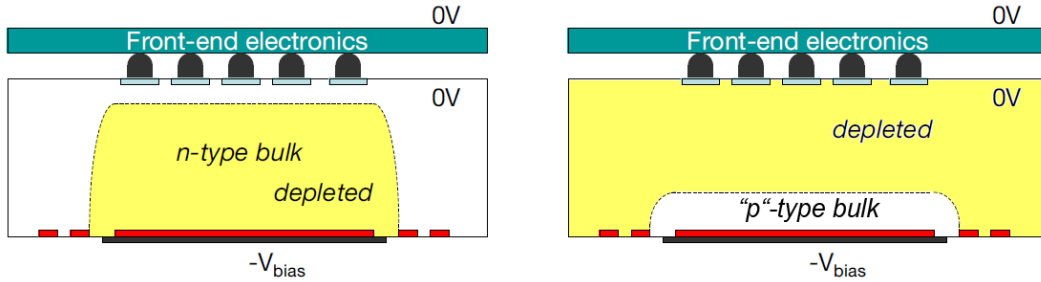
**Figure 5.1.:** Development of the depletion zone in an n-in-n sensor before (left) and after (right) type inversion. The depletion zone grows from different sides of the sensor. Before type inversion from the p-side, afterwards from the n-pixel side, that allows operation even if the sensor is only partly depleted [21].

Besides type inversion, trapping of charge carriers is another consequence of radiation damage. N-type pixels collect electrons which have a higher mobility than holes and are thus less affected by trapping. Hence, the signal height after irradiation is larger in n-in-n and n-in-p sensors than in p-in-n sensors, where holes are collected.

Due to the same doping type of the pixels and the bulk material an inter-pixel isolation is required. There are different isolation techniques [32, 26]. The three common designs are: p-stop, p-spray and moderated p-spray (see Figure 5.2). They all have an n-p-n junction to
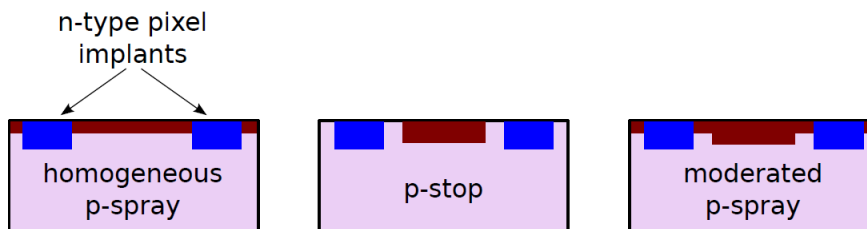


**Figure 5.2.:** Three common inter-pixel isolation techniques: p-spray, p-stop and moderated p-spray. The n-type pixels are marked in blue and the p-type isolation is coloured in red [26].

insulate the n-pixels from each other. The p-spray design adds a uniform layer, which is lowly p-type doped, on the entire pixel side of the sensor, leading to a direct contact of the n-type pixels and the p-spray implant. P-stop isolation introduces a p-type implant with high doping concentration between the n-type pixels, which requires an extra processing step. For the moderate p-spray option a p-type implant with a high concentration is used in the centre between the pixels which is surrounded by a lower moderated one. This combination of p-stop and p-spray is the best compromise between p-type concentration, electric field, processing, radiation tolerance and isolation and is currently used in the ATLAS Pixel Detector.

Each of the current ATLAS Pixel Detector n-in-n sensors [21] has a thickness of about 250 $\mu$m. In 144 columns and 328 rows, most of the pixels have a size of $400 \times 50$ $\mu$m$^2$. The maximum sensor bias voltage is -600 V due to limitations of the cables and power supplies.
The future IBL planar sensor [33] is based on the proven technology of the current ATLAS Pixel

sensor. The geometry had to be adapted to be compatible with the new FE-I4. One 200 $\mu$m thick sensor is connected to two FE chips, resulting in an array of $2 \times 80 \times 336$ pixels. Almost all pixels have a size of $250 \times 50$ $\mu$m$^2$ and the maximum sensor bias is increased to -1000 V.

## 5.2. n-in-p Design

Planar pixel sensors with p-type bulk material, that contain n$^+$ implants on the front side and a large p-type implantation on the back side, are called n-in-p sensors [34]. They have only become available recently in a quality that they can be used for tracking detectors. The n-in-p design potentially has advantages compared to the n-in-n design concerning production costs due to single-sided processing as described in the following. Cost effective sensors are important taking into account that the size of a future pixel detector depends on the cost per area. For large pixel detectors these costs have to be decreased significantly.

The absence of bulk type inversion and the fact that the main junction is between the n$^+$ pixels and the p-type bulk (see Figure 5.3) make a guard ring structure on the front side necessary. There is only a homogeneous p$^+$ implant on the high voltage back side left. Hence, the
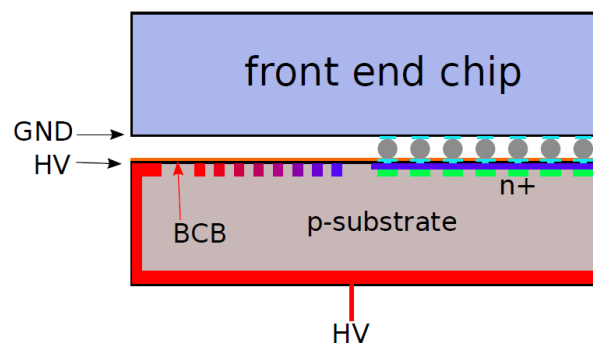


***Figure 5.3.:*** Schematic view of a n-in-p sensor, illustrating the different potentials between the sensor (HV) and the front end chip (GND) [35].

sensor needs only a structured processing from one side.

Beside this advantage in processing, an n-in-p sensor behaves similar to an n-in-n sensor. The p-spray option is used to insulate the n-type pixels and the resulting electric fields are lower and the breakdown voltage is higher compared to the moderated p-spray, which is implemented in the n-in-n technology. In addition, the depletion zone grows from the pixel side towards the high voltage pad from the beginning on and not only after type inversion.

The isolation between the front-end chip and sensor is an additional challenge compared to an n-in-n sensor. The guard ring structure is on the pixel side of the sensor (see Figure 5.3), thus the drop between the high voltage and the grounded FE chip happens on the side facing the electronics. This causes a danger of discharges between the edges of the sensor and the FE chip. Therefore, the guard ring design has to be improved and insulating materials, like Benzo Clyclo Butene (BCB), to treat the surface have to be tested.

N-in-p sensors are not yet used in high-energy particle physics due to the short availability. But especially for future large scale upgrades like the replacement of the current ATLAS Pixel

Detector this design is very promising with regard to radiation hardness and cost effectiveness.

## 5.3. Thin Sensors

Beside the different bulk dopings of the sensor, the thickness of the sensor is an aspect which can provide improvements. In most detectors in high-energy particle physics the tracking detector is surrounded by a calorimeter to measure the energy of particles. The material budget between the collision point and the calorimeter has to be as small as possible in order not to falsify the energy measurement. The thinner the sensors the less material a particle has to pass. Furthermore, multiple-scattering is suppressed, which means improved track resolution.

A thinner sensor [36] has a higher electric field at the same voltage. A better charge collection efficiency at highest irradiation is a consequence, especially if the maximum operational voltage is fixed due to the danger of discharges to other detector parts and the leakage current. Furthermore, charge multiplication effects can amplify the signal and a lower collection time decreases the possibility for trapping. Consequently, after irradiation the signal is larger compared to thicker sensors.

Figure 5.4 shows the collected charge depending on the bias voltage at two different temperatures for detectors irradiated with a fluence of $5 \times 10^{15}$ $n_{eq}$/cm$^2$. It can be seen that a 140 $\mu$m n-in-p
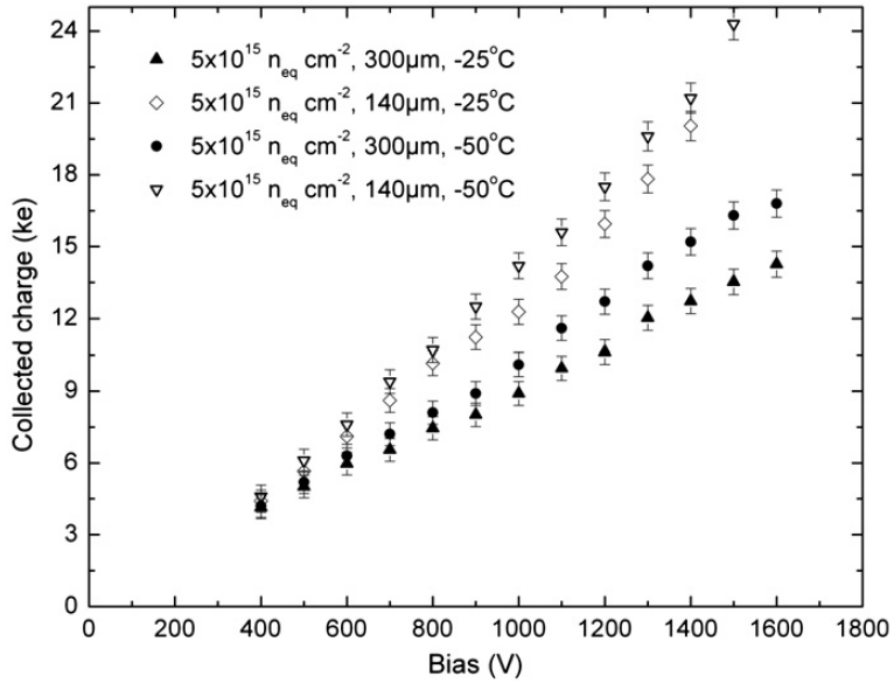


***Figure 5.4.:*** Collected charge in dependence of the bias voltage for 140 $\mu$m and 300 $\mu$m microstrip p-type detectors irradiated to $5 \times 10^{15}$ $n_{eq}$/cm$^2$, measured at $-25°$C and $-50°$C [36].

microstrip sensor collects more charge than a 300 $\mu$m sensor of the same design. Furthermore, the collected charge in the thinner sensor is higher than the expected charge of about $11200e$ for a MIP in 140 $\mu$m of silicon. This is evidence of a charge multiplication mechanism.

The process of thinning a sensor with electrically active back side was developed by the Max-Planck-Institut Halbleiterlabor [37] not so long ago. With this new technique detectors with thicknesses of down to 50 $\mu$m have been produced.

In summary, thin sensors show much better results than thicker sensors for very high fluence. This result was considered for the IBL upgrade by decreasing the thickness to 200 $\mu$m.

## 5.4. Further Designs and Technologies

In the process of developing an improved sensor design, the reduction of inactive edges of the sensor is an important point. This can be achieved by optimising the guard ring structures and reducing the safety margins between the outermost ring and the cutting edge.

For example, the planar IBL sensors [33] have a slim edges design, which reduces the inactive edges from 1100 $\mu$m to $\sim$ 200 $\mu$m. Therefore, the number of guard rings is reduced and the safety margins are narrowed. Furthermore, the edge pixels are extended beyond the high voltage pad. A different approach is an active edge, which has implants on the cutting edges to avoid conductivity.

In addition, the effects of radiation damage differ for different sensor materials. Oxygen enrichment of the silicon bulk reduces changes of the effective doping concentration.

In the current ATLAS Pixel Detector, oxygen rich float-zone silicon is used. This material is expected to extend the lifetime of the B-layer from an operation time of three years to ten years [38].

The designs described previously are planar pixel sensors. This technology is most commonly used in current experiments. Therefore, it is well understood and the standard processing allows high production yields. There are many suppliers so the costs are low. Furthermore, there is a lot of experience with the design of planar pixel sensors and a lot of optimisation work has already been done.

But after high irradiation, the leakage current increases and the signal decreases, thus new concepts are being developed.

One possible new technology is silicon 3D sensors [39, 40]. Pillars are etched into the bulk and filled with doped silicon to form electrodes. This design decouples sensor thickness and charge collection distance. Due to the short distance between the bias and the charge collecting electrode ($\sim$ 75 $\mu$m) the depletion voltage is very low, causing only a low leakage current.

The full sensor thickness can be used to collect signal charges, resulting in a larger signal. In addition, the edges can be used actively, because no guard rings are needed.

On the other hand, the 3D design needs non-standard processing which means higher costs and a lower yield. The problem of irradiation-induced defects is still present, although depletion voltage and thus leakage current are significantly reduced.

About one quarter of the sensors of IBL have a 3D design.

Diamond [41, 42] is another possible material for a sensor. It has a large band gap and thus a high displacement threshold. Even after irradiation the leakage current is very low so that cooling is not necessary and the sensor can be operated at room temperature. The low capacity due to the lower dielectric constant reduces the noise of the sensor. But because of the large band gap the signal induced by a particle is lower than in silicon.

Despite the fact, that price of diamond is very high and there is no good availability diamond is an ideal material for high radiation environments due to its material properties.

With the IBL upgrade a Diamond Beam Monitor (DBM) is added to the ATLAS detector. 24 diamond sensors with a size of 4 cm$^2$, which are connected to FE-I4 chips, are installed in the high $\eta$ region to monitor the bunch-by-bunch luminosity and beam spot. This is the largest diamond tracker that was ever built.

# 6. Measurement Setup and Scans

In order to characterise the behaviour of silicon pixel sensors with different designs before and after irradiation, a laboratory read-out system is needed. This system allows configuring the test assembly, to perform standardised tests and to develop special tests.

To test new sensor designs more functionality is required as for detector operation. The USBpix read-out system, which is a modular test system, fulfils these criteria and provides a high level of flexibility.

In the following, the USBpix system and its components are described as well as the scans that can be executed with the system.

## 6.1. USBpix Read-Out System

The compact USBpix system [43, 44] (see Figure 6.1) is a read-out system for FE-I3 and FE-I4 chips. The hardware and software components have a modular structure in order to provide large flexibility.
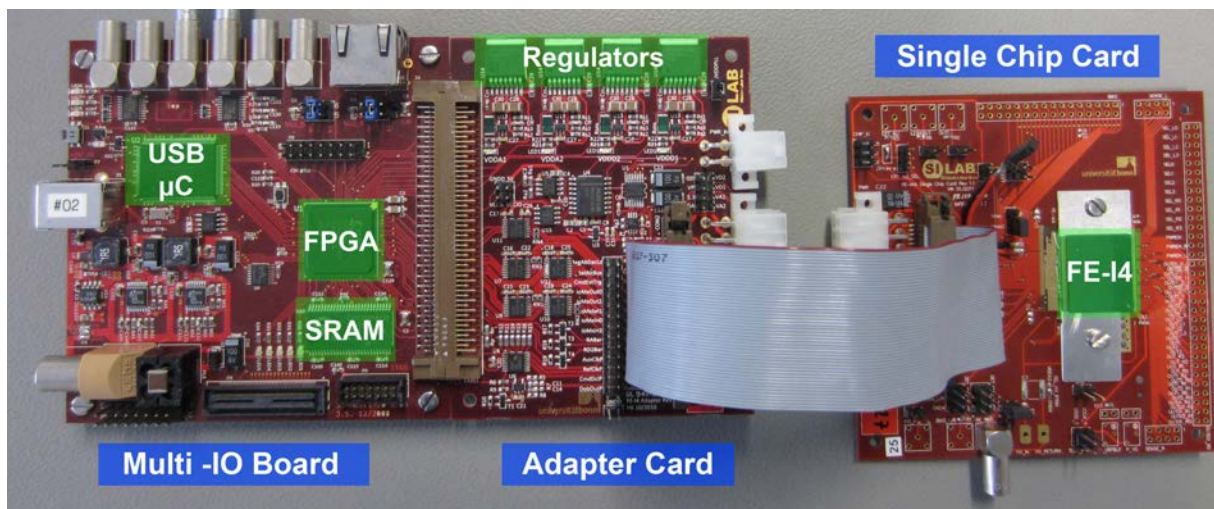


***Figure 6.1.:*** Picture of a USBpix read-out system with Multi-IO board, Adapter Card and Single Chip Card with FE-I4.

The hardware contains a multi-purpose Field Programmable Gate Array (FPGA) card with a USB2.0 interface. This Multi-IO board holds a micro controller, an FPGA and 2 MB of on-board memory (SRAM). The micro controller handles the scan routines. The FPGA controls all signals going to the FE, like configuration commands, and stores data coming from the FE in the memory. Thus, standard scan routines can be executed without communication to the PC, saving processing time.

An Adapter Card is connected to the Multi-IO board, which is dedicated to the specific flavour

of the read-out chip. The card for the FE-I4 contains voltage regulators to power the front end. The output of the regulators can be set by the user.

Via a flat ribbon cable, that routes all data and power lines, the Adapter Card is connected to the Single Chip Card (SCC). The assembly of sensor and FE chip is wire bonded to the SCC, which is a support card. The SCC allows monitoring various signals and supply voltages.

To access the hardware, an application software for USBpix is needed. It is a collection of C++ classes based on the ATLAS PixLib package, providing an interface to configure and operate the connected assembly.
STcontrol is the graphical user interface, based on ROOT and Qt. Using STcontrol chip configurations can be loaded, accessed, changed and the different scan routines can be executed. A data analysis tool called Module Analysis completes the software package.

## 6.2. Standard Scans

To compare the behaviour of different sensors it has to be taken into account that the sensor is connected to a front end chip. The calibration and the tuning of the FE has to be well understood in order to define the threshold of the discriminator and the ToT and thus hits and collected charge.
In the following, some of the standard scans [45], which are included in STcontrol, are explained. The values that are changed during the scans are explained in more detail in Section 3.3. Examples for resulting plots can be found in Chapter 7.

**Analog and Digital Test**   Via the external charge injection circuit a defined charge can be injected several times directly into the discriminator (Digital Test) or the amplifier (Analog Test) of each pixel. These tests show if the analogue and the digital part of a pixel cell work as expected, comparing the charge which is injected and read back. The read-out should report the same number of hits, if the pixel is fully functioning.
In order not to have a too high occupancy, the charge is not injected into all pixels at the same time. Masks select the double columns which are read out at the same time. The preset mask for Digital and Analog Tests injects charge at the same time in every sixth pixel. The mask is shifted by one pixel and the whole double-column is scanned after six steps.

**Threshold Scan**   The discriminator in the pixel cell compares the signal from the sensor to an adjustable threshold. Some of the fundamental scans are the determination and the tuning of this threshold. The first is realised by an algorithm called Threshold Scan.
During this scan charge is injected into the analogue part of the FE multiple times. This procedure is repeated with different charges, controlled by the `PlsrDAC`. Ideally, the result of the scan would be a step function with no hits if the injected charge is below the threshold and if it is above threshold the number of injections is equal to the number of hits. Due to noise effects, charge values close to the threshold will sometimes cause a hit and sometimes not. Figure 6.2 shows a possible result of a Threshold Scan. The data is fitted with a convolution of a step function and a Gauss function, describing the hit probability $p_{\text{hit}}$

$$p_{\text{hit}}(Q) = \frac{1}{2}\text{Erfc}\left(\frac{Q_{\text{thresh}} - Q}{\sqrt{2}\sigma_{\text{noise}}}\right), \tag{6.1}$$
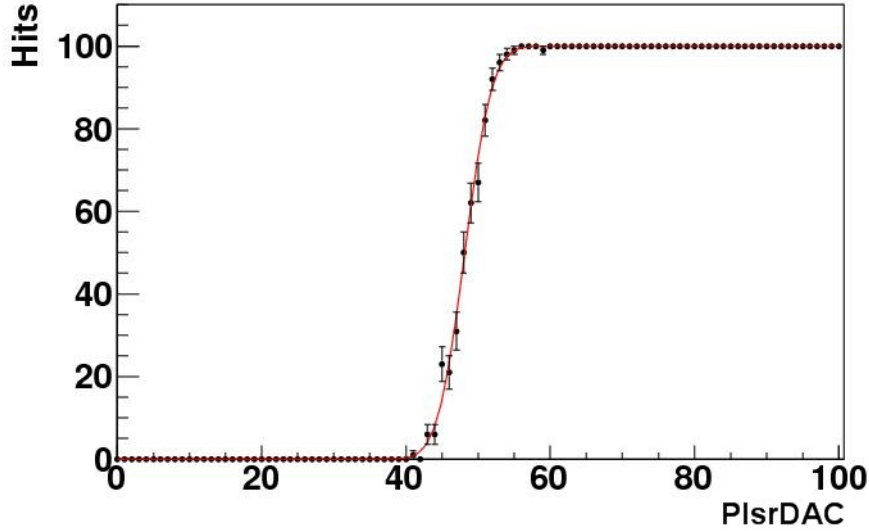
***Figure 6.2.:*** Result of a Threshold Scan. Number of hits versus the `PlrsDAC` value, parameterising the injected charge and fitted with Equation 6.1.

where $Q$, the charge of the injected pulse, is given in DAC units, $Q_{\text{thresh}}$ is the charge which corresponds to the discriminator threshold and $\sigma_{\text{noise}}$ is the equivalent noise charge (ENC) of the detector-amplifier system. Erfc is the complementary error function defined by

$$\text{Erfc}(x) = 2 \int_x^\infty e^{-x'^2} \mathrm{d}x' / \sqrt{\pi}.$$

This function is referred to as S-curve.

The resulting threshold $Q_{\text{thresh}}$ and noise $\sigma_{\text{noise}}$ of this scan are stored in two plots (SCURVE_MEAN and SCURVE_SIGMA) organised in three parts (see Figure 6.3). The top part shows the analysed value, like the number of hits or the threshold, in a colour-coded pixel map. In the middle the values for all pixels are histogramed and in the bottom there is a scatter plot, which contains the value against an identification number defined by channel=row+336*column+26880*chip. These histograms have a certain width, named dispersion, which represents the difference of the values between the single pixels and is supposed to be as small as possible, requiring tuning.

**Calibration Scans**   Before the discriminator threshold is tuned to a certain value, the charge injection mechanism has to be calibrated. The voltage step which is applied to the injection capacitors is controlled by the `PlsrDAC` value. The injected charge $Q_{\text{inj}}$ is

$$Q_{\text{inj}} = C_{\text{inj}}(\texttt{PlsrDAC} \cdot V_{\text{Grad}} + V_{\text{offset}}), \tag{6.2}$$

with the chosen injection capacitor $C_{\text{inj}}$, the conversion factor $V_{\text{Grad}}$ and a calibration offset $V_{\text{offset}}$. How the last two values are determined is described in the following.

The DAC Scan is an example for a scan that reads a value from a Detector Control System (DCS) device, which is connected to a pin on the SCC. For the calibration of the injected charge, the `PlsrDAC` is scanned and the generated voltage is measured. With the `Colpr_Addr`
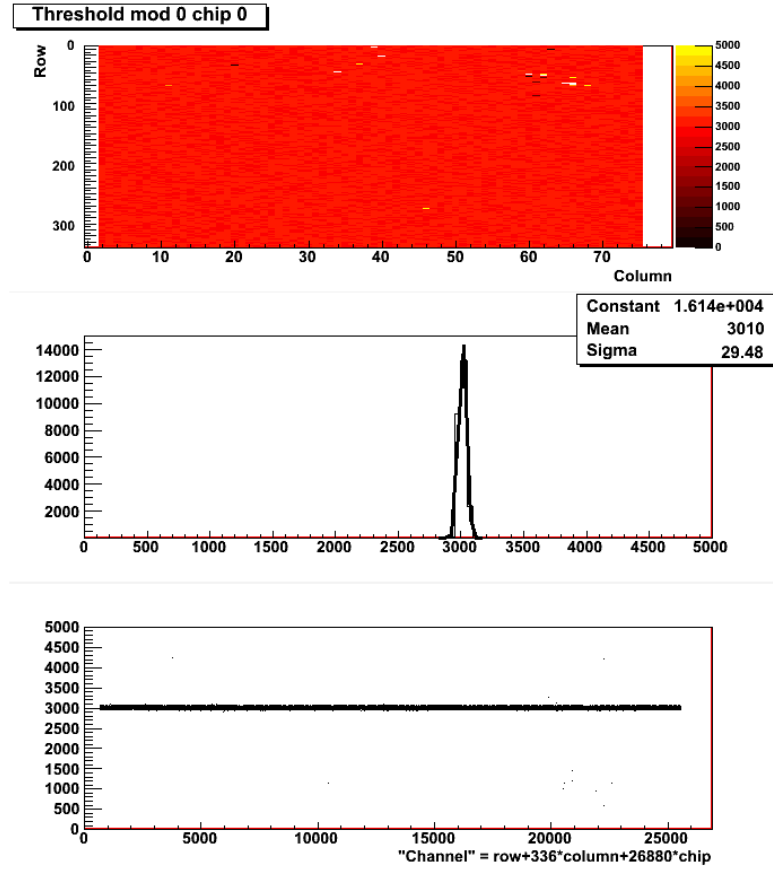
***Figure 6.3.:*** Example for a resulting plot of a Threshold Scan including a colour-coded pixel map (top), a histogram with the threshold distribution (middle) and a scatter plot (bottom).

value it can be chosen at which double-column the scan starts and injects charge. Moreover, different scan modes selected are implemented and can be chosen by the `Colpr_Mode` value, which is coded as it can be seen in Table 6.1. There is a linear dependence between `PlsrDAC`

| Colpr_Mode | Action |
| --- | --- |
| 0 | Scan only the addressed double-column |
| 1 | Scan every 4$^\text{th}$ double-column |
| | with such phase as to include addressed double-column |
| 2 | Scan every 8th double-column |
| | with such phase as to include addressed double-column |
| 3 | Scan all double-columns |

***Table 6.1.:*** Different scan modes for the DAC Scan, that identify the double-columns to be scanned [46].

and the measured voltage and the gradient is the conversion factor $V_\text{Grad}$ from DAC units into volts, which typically has a value of 1.5 mV/DAC.

In addition, the injected charge has an offset

$$Q_\text{offset} = C_\text{inj} \cdot V_\text{offset},$$

which needs to be taken into account. Therefore, the Injection Calibration Scan is performed, executing three Threshold Scans with different capacitors ($C_0$, $C_1$ and $C_0 + C_1$). This allows determining the offset voltage very accurately. Typically, the offset is in the order of 20 mV.

**Threshold Tuning**   The global value of the threshold can be adjusted with a GDAC Fast Tune procedure, which changes the `Vthin_Alt_Coarse` and `Vthin_Alt_Fine` values until the desired threshold is reached. This is determined by injecting a charge corresponding to the target threshold and monitor the hit occupancy. If the percentage of injections that result in a hit is less than 50% the value is decreased by a certain step size and if it is more than 50% it is increased. After a fixed number of iterations, during which the step size decreases, the final `Vthin_Alt_Coarse` and `Vthin_Alt_Fine` values are entered into the FE configuration.
At this stage, the threshold still has a dispersion of about $500e$ to $700e$ due to the differences between the pixels, which is large compared to the desired threshold values between $800e$ and $3000e$. This in-pixel adjustment can be done by a TDAC Fast Tune procedure, which works like the scan for the global parameter.

**FDAC Tune**   The purpose of the `FDAC` tuning is an in-pixel adjustment of ToT response to a certain charge, for example ToT=10 at a charge of $15000e$. Before executing this scan the global feedback current `PrmpVbpf` and the `FDAC` step size `FdacVbn` are selected as described in [47]. Subsequently, the `FDAC` is scanned and the ToT response to the fixed charge injection is measured. The best matching value for each pixel is chosen and entered into the FE configuration.

**Crosstalk Scan**   In a Crosstalk Scan the number of hits in a pixel is measured, while injecting charge into the two neighbouring pixels. It is performed in a similar way as the Threshold Scan, but here the injection mask is different to the read-out mask. The injection is applied to the neighbours in the same column, which are the ones on the long side edge.

**Source Scan**   In order to test the assembly with a radioactive source a Source Scan is performed. The radiation from the source produces electron-hole pairs in the sensor material, which are measured instead of the charge signal from the pulser. The data taking is activated by different trigger sources, from which two are used for the experiments in Chapter 7.
At first, the trigger signal can be generated by the hitbus, which forms a coincidence of the discriminator output of all pixels. Thus, it indicates a hit anywhere on the chip. Noisy and stuck pixels, which disable the hitbus, have to be masked in order not to use them for triggering. Stuck pixels can be found with the Stuck Pixel Scan.
Secondly, an external trigger signal from a scintillator below the assembly can be used to assure that the hit was caused by a MIP passing the sample. The scintillator output can be shaped with an external discriminator, so that only hits above a certain noise level cause a trigger signal. After a preset number of triggers, the event information is written into an ascii-file, referred to as raw data file (see Figure 6.4). Every external trigger is marked with the letters TD (green box) and every data header (DH) contains a new bunch-crossing identifier (BCID) to synchronise with the rest of the ATLAS subdetectors. The hit information is transmitted in the data record (DR, red box). After the DR there is the hit information of column and row and the $\text{ToT}_{\text{Code}}$ for pixel (col,row) and a second $\text{ToT}_{\text{Code}}$ for the pixel (col,row+1). The translation can be seen in Table 6.2.
Hits with low charge deposition can be delayed to the particle crossing by the timewalk effect. The FE-I4 allows recovering these by indicating the presence of a delayed hit in the correct

| 4 | 0xf84000 | 12 | DH 0 86 60 | 20 | DR 22 269 2 15 | 28 | DH 0 86 67 | 36 | DH 0 86 71 |
| 5 | 0x000001 | 13 | 0xe9563d | 21 | 0xe95640 | 29 | 0xe95644 | 37 | 0xe95648 |
| 6 | TD 2 0 1 | 14 | DH 0 86 61 | 22 | DH 0 86 64 | 30 | DH 0 86 68 | 38 | DH 0 86 72 |
| 7 | 0xe9563a | 15 | 0xe9563e | 23 | 0xe95641 | 31 | 0xe95645 | 39 | 0xe95649 |
| 8 | DH 0 86 58 | 16 | DH 0 86 62 | 24 | DH 0 86 65 | 32 | DH 0 86 69 | 40 | DH 0 86 73 |
| 9 | 0xe9563b | 17 | 0xe9563f | 25 | 0xe95642 | 33 | 0xe95646 | | |
| 10 | DH 0 86 59 | 18 | DH 0 86 63 | 26 | DH 0 86 66 | 34 | DH 0 86 70 | | |
| 11 | 0xe9563c | 19 | 0x2d0d2f | 27 | 0xe95643 | 35 | 0xe95647 | | |

**Figure 6.4.:** Snapshot of the output file of a Source Scan for one external trigger (TD, green box) with one hit (DR, red box) in pixel (22,269) with $\text{ToT}_{\text{Code}}$=2 at BCID=6.

| $\text{ToT}_{\text{Code}}$ | 0-12 | 13 | 14 | 15 |
|---|---|---|---|---|
| ToT [25 ns] | $\text{ToT}_{\text{Code}}$+1 | >13 | delayed hit | no hit |

**Table 6.2.:** Translation from the $\text{ToT}_{\text{Code}}$ value to real ToT value.

BCID.

The structure of this file is important for the analysis. In order to get a histogram, which shows the charge spectrum of the radioactive source, the ToT value has to be converted into charge (see Section 6.3) and the hits need to be clustered. If the particle passing the sensor produces charge carriers in two or more neighbouring pixels, this charge needs to be summed up and entered as one charge cluster into the histogram.

During the work for this thesis a clustering algorithm was developed, which takes into account the second ToT value as well as delayed hits and produces a clustered charge spectrum and histograms for the cluster size and a BCID distribution. Figure 6.5 shows a comparison of a $\text{ToT}_{\text{Code}}$ spectrum for americium 241, which is a $\gamma$-source, before (red) and after (blue) clustering. The histogram is shifted to larger $\text{ToT}_{\text{Code}}$ and the number of entries has decreased due to
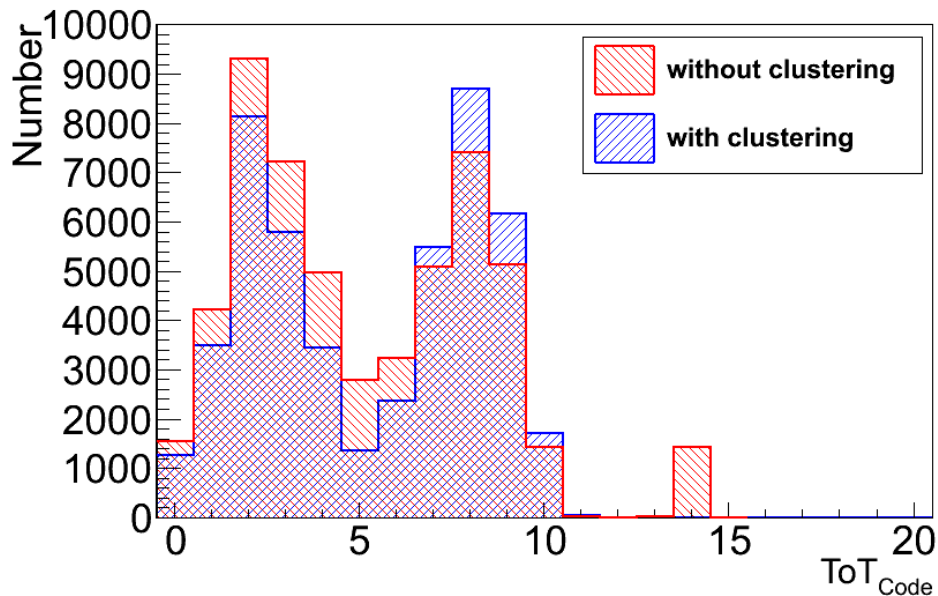


**Figure 6.5.:** Comparison of an americium 241 spectrum without (red) and with (blue) clustering, causing a shift to larger $\text{ToT}_{\text{Code}}$ and a reduction of the number of entries.

the clustering. The peak at $\text{ToT}_{\text{Code}} = 14$ is indicating the number of delayed hits.

**Noise Occupancy Scan** There are not only hits due to particles, but noise hits as well. A Noise Occupancy Scan works in principle like a Source Scan without source and uses a fixed frequency trigger which is not related to the hitbus signal. Only the occupancy due to noise events is recorded and no raw data file is produced.

With the Noise Occupancy Scan the noise of the module is observed with a better resolution compared to the Threshold Scan and thus a more realistic picture of the noise is created.

**Current-Voltage Characteristic** So far, the described scans are testing the FE and only using the sensor for charge production. The IV-Scan measures the current-voltage characteristic of a sensor. Therefore, the sensor bias voltage is varied and the resulting leakage current is measured.

## 6.3. Development of a Novel Charge Calibration

In a Source Scan the ToT value of a charge signal is measured, which has to be converted to a real charge value. This is the motivation of the ToT Calibration Scan for FE-I4.

The `PlsrDAC` can be converted into charge with Equation 6.2. Thus, with a connection between ToT and `PlsrDAC` a charge calibration for the ToT values can be done. To make this calibration as precise as possible, the connection between the two values is done for every pixel.

In order to create this connection between `PlsrDAC` and ToT, a new scan for STcontrol was developed during the work for this thesis. This scan produces three parameters $a$, $b$ and $c$ for each pixel to convert ToT into charge by using

$$Q = a + b\mathrm{ToT} + c\mathrm{ToT}^2. \tag{6.3}$$

The idea of the scan and the subsequent evaluation is first described for a single pixel.

The scan consists of several steps. At each step, a certain charge is injected into the pixel by the `PlsrDAC` . For each injection at this `PlsrDAC` value the result for the pixel is one of 16 possible ToT. Typically 200 different charges are injected, every charge 50 times.

The scan result is the number of hits for each ToT and each `PlsrDAC` , thus

$$200 \text{ \texttt{PlsrDAC}} \cdot 16 \text{ ToT} = 3200 \text{ Pixel Values.}$$

For the evaluation each pixel is considered individually. For a fixed ToT, all pixel values for the different `PlsrDAC` values in a single pixel are gone through. The `PlsrDAC` values containing this ToT are averaged using the arithmetic mean (see Figure A.1 in the Appendix). The mean `PlsrDAC` is then converted into charge with the normal `PlsrDAC` calibration (see Equation 6.2). This process is repeated for all ToT values.

For each pixel, a plot is obtained (see Figure 6.6), which associates an average charge $Q_{\mathrm{mean}}$ to each ToT. The ToT value is $\mathrm{ToT}_{\mathrm{Code}}$ and due to the special meaning the values (see Table 6.2) larger than twelve are not considered for the calibration. The data are fitted with a second order polynomial as shown by Equation 6.3. The resulting three parameters are stored in the corresponding histogram.

This procedure is done for all pixels. An example of one of the parameter histograms can be seen in Figure 6.7. Using these histograms the ToT values from the Source Scan can be converted into charge.
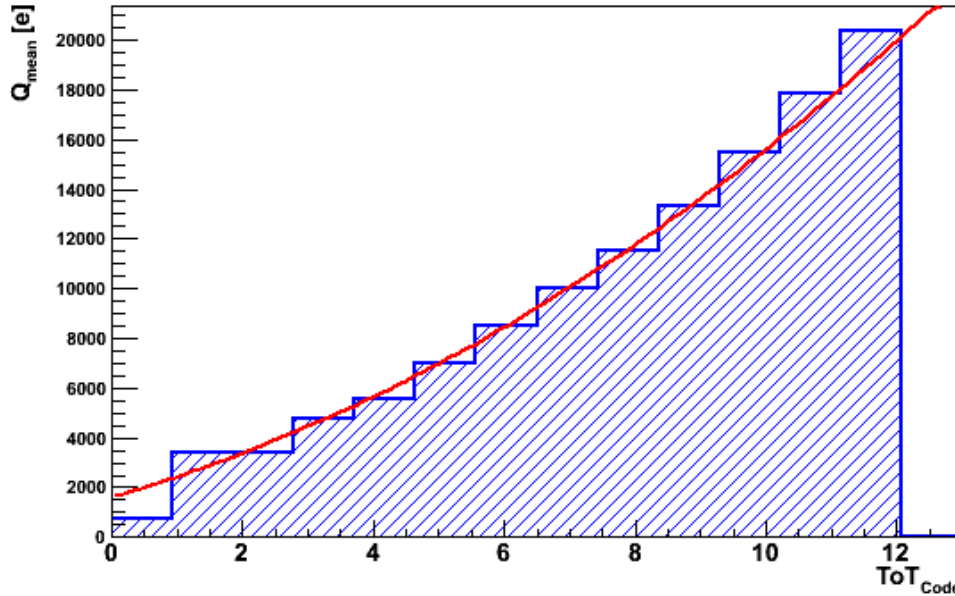
**Figure 6.6.:** Dependence of mean charge $Q_{\mathrm{mean}}$ on $\mathrm{ToT}_{\mathrm{Code}}$ for one pixel. The histogram is fitted with a second order polynomial.

The ToT Calibration is tested with different $\gamma$-sources and charge injections into a n-in-p sensor (ToT Verification Scans). Figure 6.8 shows the result for the measured charge versus the expected charge. The observed charges for the Source Scans with americium 241, cadmium 109 and cobalt 57 (blue) are larger than the expected values. For the charge injections (red) with a given charge the values below the `FDAC` tuning point are too large and above too small. At the tuning point of 10 ToT at 15,000$e$ both values agree. The gradient of the two linear fits are comparable and in the order of 1.4, but the intercept is significantly different.

One possible explanation is a discrepancy between the real capacities of the used capacitors and the nominal values. Unfortunately, the capacity cannot be measured directly for the FE-I4, like it was possible for the FE-I3, but indirect measurements have to be performed.
The first idea is to inject charge into one single pixel via a laser and calculate the capacitance
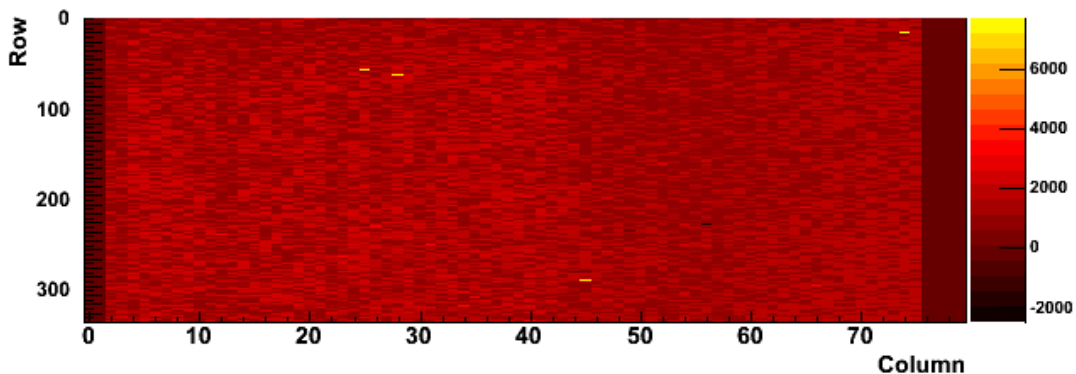


**Figure 6.7.:** Example of a parameter histogram, which is the result of the ToT Calibration Scan.
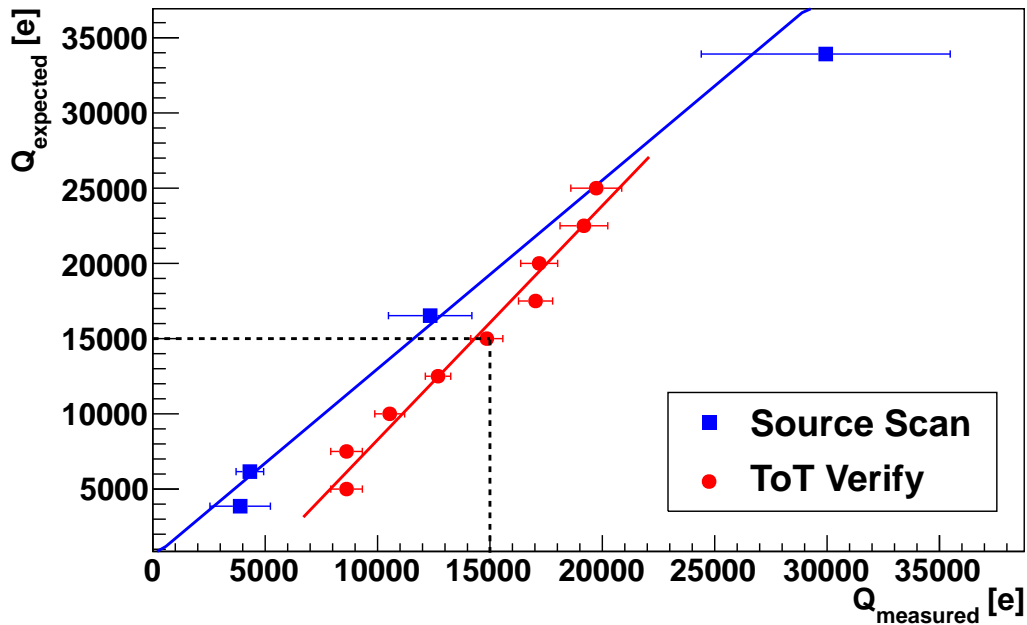
***Figure 6.8.:*** Measured versus expected charge for Source Scans (blue) with americium 241, cadmium 109 and cobalt 57 and injections of test charges for the unirradiated n-in-p sample (SCC127). For the injection of the charge of the tuning point (10 ToT @ 15,000$e$) both charges agree.

from the known injected charge and the measured. But, this method is not practicable for the n-in-p sample, because there is a handle wafer on top of the sensor, which changes the injected charge.

The second method uses the discriminator threshold to find the correct injected charge. Knowing the energy of different radioactive sources, the hit rate is measured as a function of the threshold. At low threshold the hit rate is high, because the threshold is smaller than the charge caused by the source. At the threshold which corresponds to the peak energy of the source, the hit rate drops. This point marks the number of electron-hole pairs produced by the source. Using sources with different energies the number of electron-hole pairs can be plotted versus the measured threshold and a correction factor for the capacities can be calculated. In order to observe the drop in the hit rate, the threshold needs to be tuned to a threshold close to the expected energy of the used source. This is not possible for the high energies (e.g. Co at about 34000$e$) and only one point for cadmium is recorded.

Thus the final validation of the calibration is still to be done. Until then the error of the ToT Calibration is estimated to be in the order of some 100$e$.

# 7. Results

One of the aims of this master's thesis is to compare the performance of thin n-in-n and n-in-p sensors before and after irradiation. The methods and scans described in Chapter 6 are used to test the influence of different designs on the behaviour of the samples. Table 7.1 shows some characteristics of the different sensors that are tested.

| Name | Thickness [$\mu$m] | Design | Fluence [$n_{\mathrm{eq}}/\mathrm{cm}^2$] | Radiation type |
|---|---|---|---|---|
| SCC151 | 150 | n-in-n | 0 | n/a |
| SCC127 | 150 | n-in-p | 0 | n/a |
| PS4 | 150 | n-in-n | $5 \times 10^{15}$ | 24 GeV p |
| SCC132 | 150 | n-in-p | $5 \times 10^{15}$ | 24 MeV p |

***Table 7.1.:*** Overview of the four used sensors.

The four sensors with two different bulk dopings, are mounted to FE-I4A read-out chips. Since the FE-I4A is a prototype some special features are added to the layout, in order to test different or new read-out concepts. The discriminators in the double-columns 1, 6, 11, 13, 15, 17, 22, 23, 24 and 25 (counted from 0 to 39) employ a different feedback capacitor than the others, which will be visible in some results of Threshold Scans. Furthermore, the double-columns 0, 38 and 39 are disabled for almost all scans, since they do not work as expected due to a design feature of the frond end.

At first, the results of scans with the assemblies that are not irradiated are presented and the differences are described. Afterwards, the same measurements with the irradiated samples are discussed.

## 7.1. Results of unirradiated samples

### 7.1.1. IV Measurement

The current-voltage characteristics of the two unirradiated samples is displayed in Figure 7.1. It can be seen that the absolute value of the leakage current for the n-in-n sample at a bias voltage of -150 V is $-(0.76087 \pm 0.00001)$ $\mu$A, which is about three times larger than the current of the n-in-p sample with $-(0.25069 \pm 0.00001)$ $\mu$A.

Down to a voltage of -150 V, no sudden large increase of the absolute leakage current is observable, thus both sensors show no indication of breakdown. The n-in-n sample is operated at a bias voltage of -150 V in the following. The n-in-p sensor has a BCB insulation between sensor and front end chip in order to avoid discharges. But it is chosen to operate the sensor at a bias voltage of -120 V in order not to take the risk of damaging the chip, because there is only a small amount of n-in-p sensors available. Hence, the absolute leakage current at the operating bias voltage is $-(0.16527 \pm 0.00001)$ $\mu$A for the n-in-p sample.
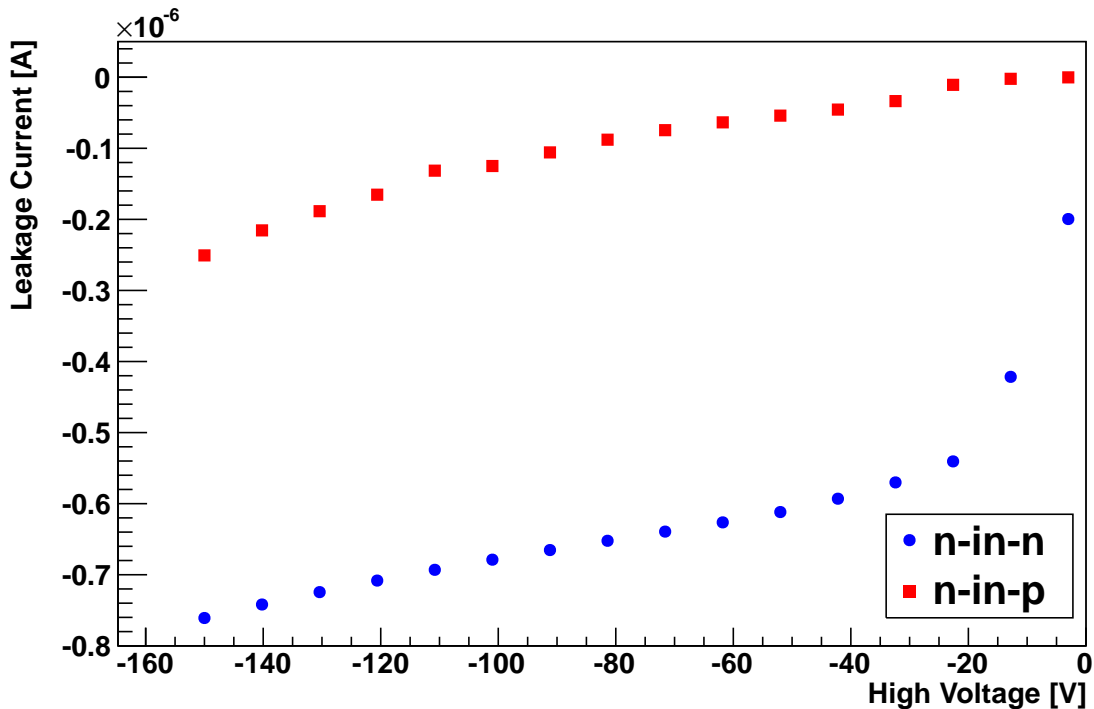
**Figure 7.1.:** Current-voltage characteristic for unirradiated n-in-n sample (SCC151, blue) and n-in-p sample (SCC127, red). At a bias voltage of -150 V the absolute value of the leakage current of the SCC151 is three times larger than the one of the SCC127. The error bars are too small to be seen.

### 7.1.2. Calibration and Tuning

Before the samples can be tuned an accurate calibration of the `PlsrDAC` has to be done. For the determination of the `PlsrDAC` gradient $V_{\mathrm{Grad}}$ different modes and starting columns are tested. Figure 7.2 shows the outcome of several DAC Scans in different modes, performed with the n-in-n sample (SCC151) in order to obtain the gradient which is entered into the FE calibration. It can be seen, that there is no significant difference between the resulting gradients, but some saturation effects occur. The saturation for small `PlsrDAC` values is due to the leakage current of a switch, which connects the `PlsrDAC` with the pixels of double-column 0. For higher `PlsrDAC` values a saturation for all tested configurations is visible. The more double columns are selected for injection at the same time the smaller the range available before the voltage for the `PlsrDAC` saturates. For the n-in-n sample the scan was started in double-column 2 and in mode 2 whereas only double-column 1 is scanned for the n-in-p sample.

To perform a usable offset determination for the `PlsrDAC` $V_{\mathrm{offset}}$, the discriminator threshold has to be high enough, so that noise does not affect the measurement. This is the case at about $3000e$.

In Table 7.2 the resulting calibration parameters can be seen, which are in the range of the expected values. The corresponding charges are calculated using the sum of the two capacitors $C_0 + C_1 = 5.8$ fF to have a better comparable quantity. There are no errors indicated, because they can not be used in the FE calibration. One `PlsrDAC` step corresponds to about $50e$ for
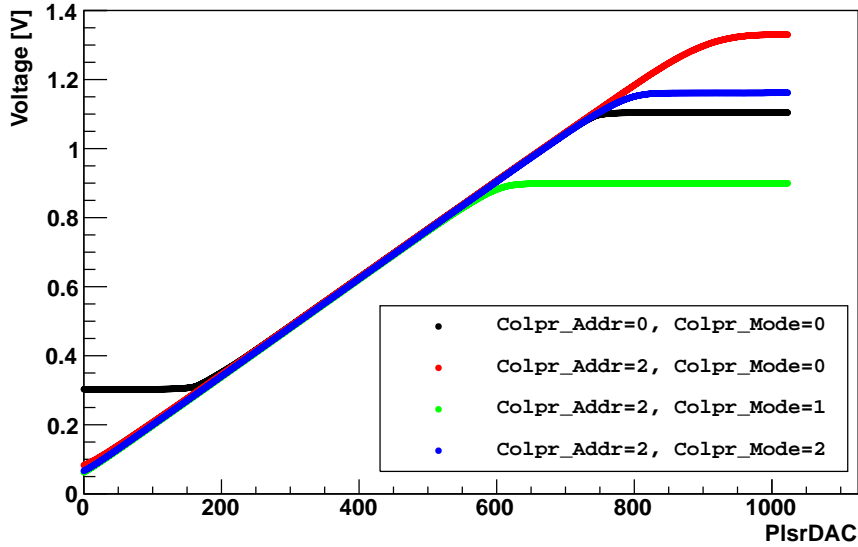
**Figure 7.2.:** Results of different DAC Scans for different configurations, recorded with the unirradiated n-in-n sample - SCC151.

|  | $V_{\mathrm{Grad}}$ |  | $V_{\mathrm{offset}}$ |  |
| --- | --- | --- | --- | --- |
|  | [mV/DAC] | [e] | [mV] | [e] |
| SCC151 - n-in-n | 1.404 | 51 | 15.8719 | 575 |
| SCC127 - n-in-p | 1.501 | 54 | 20.7672 | 753 |

**Table 7.2.:** Resulting calibration parameters determined by DAC Scans for unirradiated sensors with n-in-n (SCC151) and n-in-p (SCC127) design.

both samples and the offset for the n-in-n and n-in-p sample is $575e$ and $753e$, respectively.

Knowing the `PlsrDAC` calibration, the discriminator threshold and the feedback current can be tuned. This is an iterative process of `TDAC` and `FDAC` scans, which influence the individual settings. A `TDAC` scan changes the discriminator threshold and thus the ToT and the other way around, which can be understood by recalling Figure 3.4.

For a tuning to a desired threshold a sequence of scans is executed, composed of a GDAC Fast Tune, a TDAC Fast Tune, an FDAC Tune and a second TDAC Fast Tune scan. In order to check the single steps of the tuning, several Threshold Scans are performed. After the FDAC Tune procedure, which sets a ToT of 10 bunch crossings (bx) to a charge of $15000e$, the threshold is about $1000e$ lower, which makes a second fast `GDAC` tuning necessary, because the `TDAC` step size is not large enough to adjust this change.

Due to radiation damage the signal height produced by a particle is decreased. In order to still detect the particle, low thresholds are needed. To reach a lower threshold of $1600e$ or even $800e$, the tuning routine has to be customised. The configuration for a threshold of $3000e$ is the starting point from which the `GDAC`, meaning the `Vthin_Alt_Fine`, is decreased until a Threshold Scan shows the desired threshold. A TDAC Fast Tune scan is performed with the present `TDAC` values as start values. The dispersion of the threshold is increased by the reduction of the global threshold parameter and again decreased by the TDAC Fast Tune.

### 7.1.3. Results of Threshold Scans

For all assemblies the discriminator threshold is tuned to $3000e$, $1600e$ and $800e$ and Threshold Scans with and without applying sensor bias voltage are carried out. The results for the measurements with bias voltage are presented in Table 7.3 showing no large differences between the two samples. The desired threshold is reached for all three targets and the dispersions are small with values between $30e$ and $60e$, showing the quality of the tuning. The noise increases while going to smaller thresholds, which is a known phenomenon. For the n-in-p sample the noise is on average about $16e$ smaller than values for the n-in-n sample due to the smaller leakage current.

| SCC151 - n-in-n | | | SCC127 - n-in-p | | |
|---|---|---|---|---|---|
| Threshold [e] | Dispersion [e] | Noise [e] | Threshold [e] | Dispersion [e] | Noise [e] |
| 3010 | 29 | 131 | 3037 | 52 | 113 |
| 1608 | 29 | 140 | 1603 | 31 | 126 |
| 813 | 34 | 161 | 799 | 45 | 145 |

***Table 7.3.:*** Discriminator threshold, dispersion and noise from Threshold Scans for the unirradiated n-in-n (SCC151) and n-in-p (SCC127) sample tuned to $3000e$, $1600e$ and $800e$.

Even for a threshold of $800e$ a good tuning is possible, which can be seen in the results in Figure 7.3. For the n-in-n sample there are some pixels in the upper right corner of the pixel map that show a different behaviour. This is explained by the fact, that these pixels are noisy or not connected to the front end as it can be seen in Analog and Digital Tests. The threshold distribution for the n-in-p sample displays the behaviour of the pixels with the new design mentioned in the beginning of this chapter. In this scan these pixels are not enabled, resulting in the peak at about $500e$ in the threshold distribution. In addition, the double-columns with the different capacitances can be seen as darker regions in the pixel map and in the scatter plot having a smaller noise value.

In contrast to the measurements with sensor bias voltage, the measurements without high voltage indicate differences between the two samples. Table 7.4 illustrates the large difference in dispersion and noise for a threshold of $3000e$, where the n-in-p sample worked comparable to the scans with bias voltage. Furthermore, the values for $1600e$ and $800e$ are not measurable for the n-in-n sample. Here the consequence of the two different bulk dopings is visible, meaning the absent pixel insulation through the bulk. Without bias voltage, the n-in-n sensor is not depleted and thus the $n^+$-type pixels are short-circuited via the n-type bulk, making a threshold measurement impossible. In contrast, the $n^+$-type pixels are isolated in a p-type bulk.

### 7.1.4. Crosstalk

The crosstalk gives a measure for fake hits due to inter-pixel communication and evaluates the insulation between the pixels and through the bulk. Table 7.5 displays the number of pixels, which have hits due to crosstalk. At first the results of the Crosstalk Scans with sensor bias voltage (see Figure A.2 in the Appendix) are considered and there are no particular differences
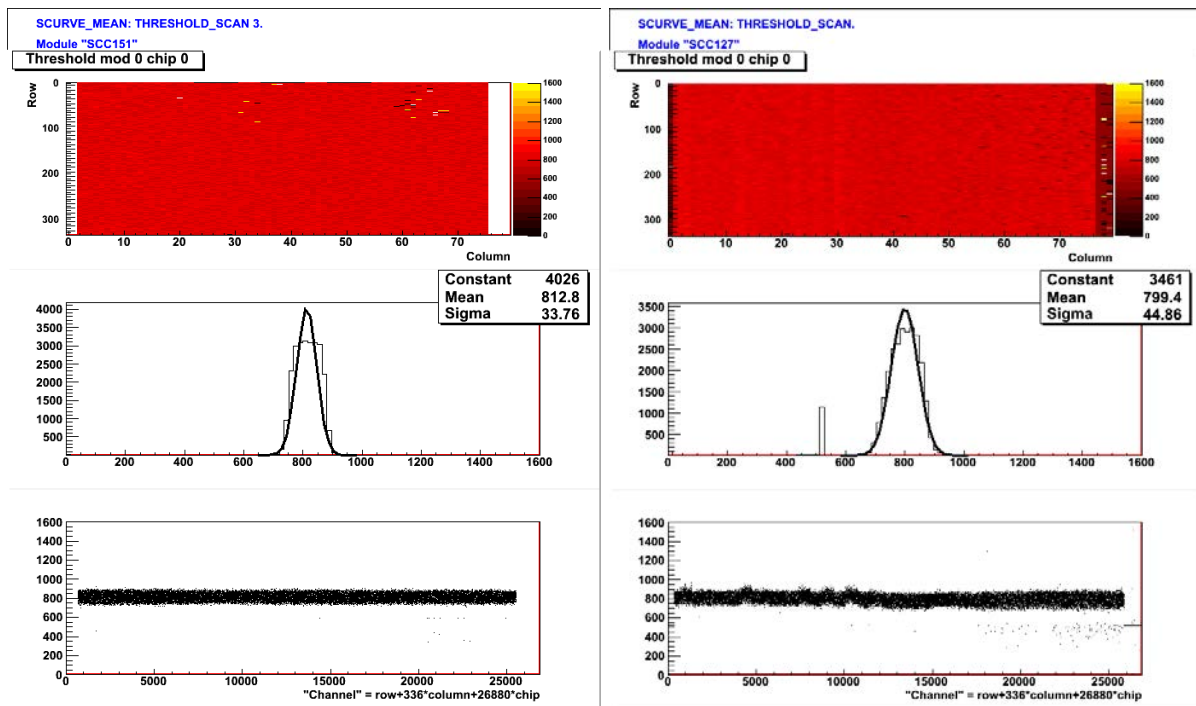
(a) Threshold for SCC151.

(b) Threshold for SCC127.
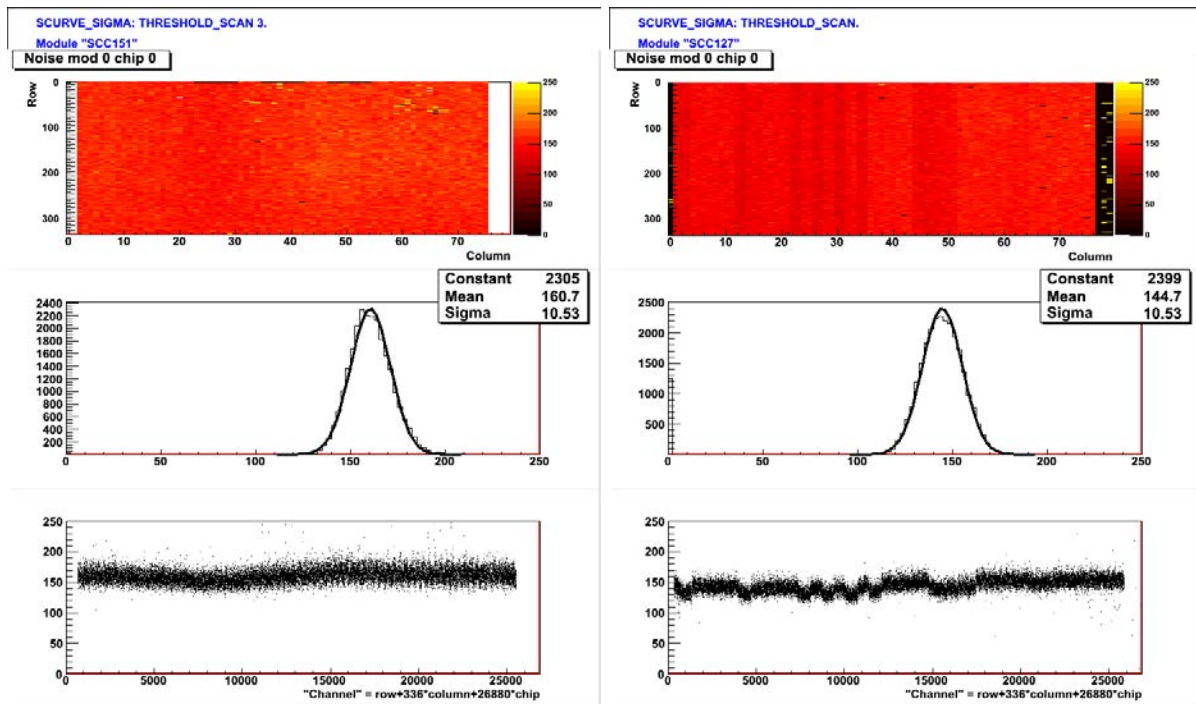


(c) Noise for SCC151.

(d) Noise for SCC127.

***Figure 7.3.:*** Resulting discriminator threshold (top) and noise (bottom) for a tuning target of $800e$ measured with the n-in-n sample (SCC151, left) and the n-in-p sample (SCC127, right) showing no difference.

| SCC151 - n-in-n | | | SCC127 - n-in-p | | |
|---|---|---|---|---|---|
| Threshold [e] | Dispersion [e] | Noise [e] | Threshold [e] | Dispersion [e] | Noise [e] |
| 3195 | 270 | 466 | 2952 | 67 | 205 |
| 1400* | 540* | 500* | 1546 | 72 | 220 |
| - | - | - | 738 | 117 | 217 |

***Table 7.4.:*** Discriminator threshold, dispersion and noise from Threshold Scans without sensor bias voltage for the n-in-n (SCC151) sample and the n-in-p (SCC127) sample tuned to $3000e$, $1600e$ and $800e$. * These values are estimations from a widely scattered pixel results.

| Threshold [e] | SCC151 - n-in-n | | SCC127 - n-in-p | |
|---|---|---|---|---|
| | Number of pixels with crosstalk | | | |
| | with HV | no HV | with HV | no HV |
| 3000 | 12 | 14 | 0 | 0 |
| 1600 | 25 | 13369 | 7 | 7 |
| 800 | 329 | 21942 | 1077 | 20008 |

***Table 7.5.:*** Number of pixels with hits due to crosstalk for the unirradiated n-in-n (SCC151) and n-in-p (SCC127) samples at thresholds tuned to $3000e$, $1600e$ and $800e$. Crosstalk Scans are performed with and without sensor bias voltage (HV).

between the two different bulk dopings. Looking at thresholds tuned to $3000e$ and $1600e$, the number of hits is below 30, which is about one per mill of the total number of pixels. Most of these pixels are damaged for example due to incorrect bump connections and are masked out in the following scans.

At a threshold of $800e$ about 2% and 4%, respectively of the n-in-n and n-in-p pixels have a hit. This is due to the low threshold, which is closer to a charge signal created by noise.

For the tests without bias voltage the characteristics of the two samples diverge, as it is already observed in the Threshold Scans. In the n-in-n sample 50% to 80% of the pixels have a hit at the lower thresholds, whereas the n-in-p sample at a threshold of $1600e$ shows only very few hits. At a threshold of $800e$ even the n-in-p sample shows hits in almost all pixels, due to the very low threshold.

### 7.1.5. Noise Occupancy

In order to get an estimation of the hits caused by noise, Noise Occupancy Scans are performed at different threshold and bias voltage settings. The results can be seen in Figure 7.4, presenting the data for the n-in-n design in blue and for the n-in-p design in red.

In the top left of this figure the noise occupancy normalised to the number of triggers and pixels versus the discriminator threshold is illustrated. The number of sent triggers is $10^9$, thus the noise occupancy cannot be smaller than the inverse of this value. Each Noise Occupancy Scan produces a histogram, which contains the noise occupancy values for all pixels. These values differ a lot for single pixels, which can be seen by the large errors, which are the root mean square of all entries. The data point itself is the mean value of all histogram entries. If the noise occupancy of single pixels extends a value of $10^{-5}$, it is masked and not considered for the mean value.

(a) Noise occupancy versus threshold.



(b) Noise occupancy versus bias voltage.



(c) Number of masked pixels versus threshold.



(d) Number of masked pixels versus bias voltage.
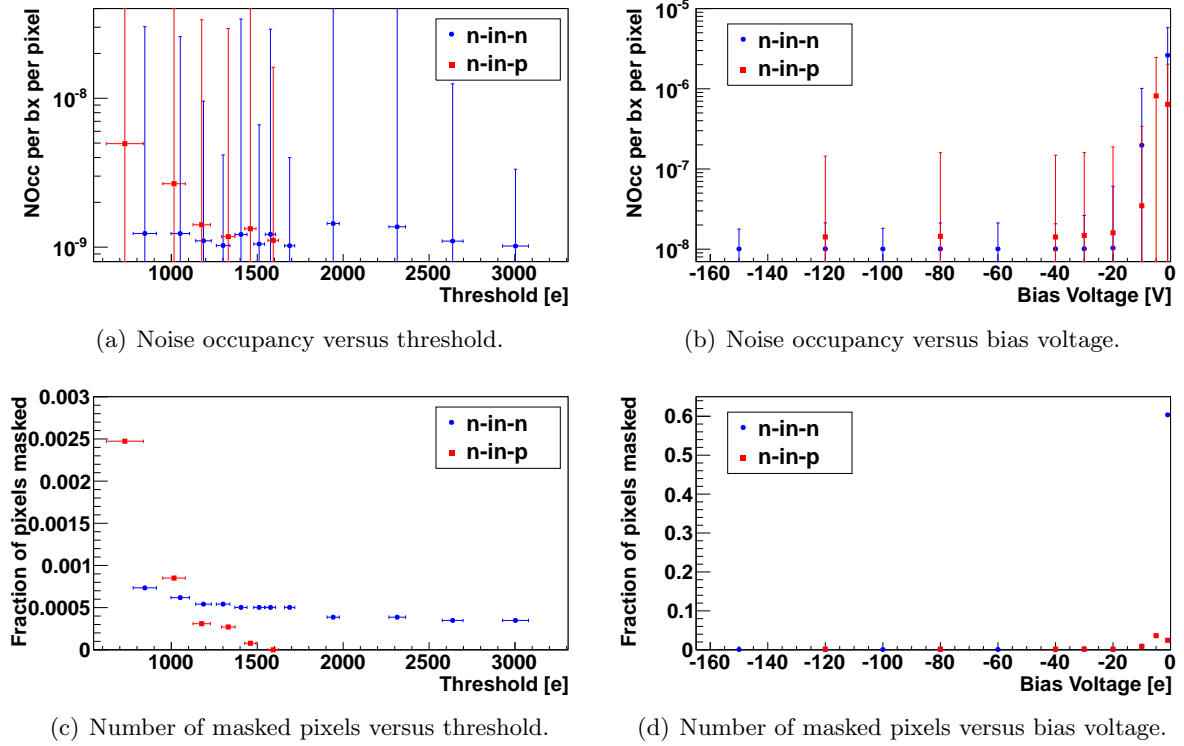
**Figure 7.4.:** Noise occupancy per bunch crossing (bx) and pixel (top) and number of masked pixels (bottom) versus threshold (left) and sensor bias voltage (right) for the unirradiated n-in-n (SCC151, blue) and n-in-p (SCC127, red) sample.

For the n-in-n sample the mean noise occupancy is constant at a value of about $10^{-9}$, whereas an increase of the noise occupancy with decreasing threshold is visible for the n-in-p sample. Despite the large errors, this behaviour is confirmed by the number of masked pixels, which can be seen in the bottom left plot. The number of pixels which are masked for the n-in-n sensor for very low thresholds is smaller than the number for the n-in-p sample. Even for higher thresholds the n-in-n sample shows a constant number of about 15 pixels that are masked. These are the same pixels that could be seen in the Crosstalk Scan and which are not working properly.

So far, the Noise Occupancy Scans were performed at the denoted sensor bias voltage. In the following, the bias voltage is varied and the effects on the noise occupancy are studied by sending $10^8$ triggers. For voltages up to -20 V the noise occupancy is constant at a value of about $10^{-8}$, which is supported by the number of masked pixels. For smaller absolute voltage values the noise occupancy increases up to $10^{-6}$ for both assemblies and 60% of the n-in-n pixels are masked, but only about 3% of the n-in-p pixels.

This behaviour is explained by the development of the depletion zone. For the n-in-p sample the depletion zone starts at the pixel side, thus the pixels are isolated at very low bias voltages. The noise occupancy decreases faster with a decreasing bias voltage compared to the noise occupancy for the n-in-n sample. But, as it can be seen later, the depletion voltage for the n-in-n sample is lower than the depletion voltage for the n-in-p sample, making the difference in the behaviour of the noise occupancy smaller.

### 7.1.6. Measurements with Radioactive Sources

Before performing any Source Scans it is important to mask stuck and noisy pixels, in order to make a triggering with the hitbus signal possible. Otherwise, the hitbus is disabled and no triggers can be counted. About 20 pixels are masked for the n-in-n sample and 5 pixels for the n-in-p sample.

At first, Source Scans are performed, which are triggered with the hitbus indicating a hit anywhere on the chip. A radioactive source is put into a special safe, which is shielded and contains the assembly located below the source. 50,000 triggers are sent for the measurements with the three available $\gamma$-sources, americium 241 (Am), cadmium 109 (Cd) and cobalt 57 (Co).
The resulting charge spectra of these Source Scans can be seen in Figure 7.5 and the $\text{ToT}_{\text{Code}}$-spectra can be found in the Appendix in Figure A.4. Raw data files produced by a Source Scan contain the ToT information, which is converted into charge using the parameters from the ToT Calibration Scan as described in Section 6.3. The peak values, determined by a Gaussian fit, are marked in the plots and can be found in Table 7.6. For Co the peak was fitted from the histogram which only contains hits with a cluster size of two, because there the peak is more distinct. The dominant error of these values is the uncertainty of the ToT Calibration which is estimated to be in the order of some $100e$. The expected charge corresponds to the energy of the $\gamma$-spectrum line with the highest intensities.

| Isotope | $E_\gamma$ [keV] | $Q_{\text{expected}}[e]$ | $Q_{\text{SCC151}}[e]$ | $Q_{\text{SCC127}}[e]$ |
|---------|------|------|------|------|
| Am-241 | 13.9 | 3861 | 4300 | 3900 |
|  | 59.5 | 16527 | 13500 | 12300 |
| Cd-109 | 22.2 | 6160 | 4800 | 4300 |
| Co-57 | 122.1 | 33916 | 29900 | 26500 |

**Table 7.6.:** Overview of the $\gamma$-spectra peak values obtained with the unirradiated n-in-n (SCC151) and n-in-p (SCC127) sample. The most intensive $\gamma$-energies are from [48]. The errors of the measured values are expected to be some $100e$ due to the ToT Calibration.

The different spectra for the two samples, which are tuned to the same values, have no significant difference in the shape. Taking into account the large errors of the ToT Calibration, the peak values are comparable.

Besides the measurements with the three $\gamma$-sources, strontium 90 (Sr) as a $\beta^-$-source is used to measure the depletion voltage of the sensors. Electrons with an energy of 546 keV and 2.3 MeV [48] are emitted. Several Source Scans at different sensor bias voltages are executed and the resulting peak value of the spectrum is plotted against the voltage. If the total charge is collected the sensor is completely depleted.
These Source Scans are triggered using a scintillator, which is located below the assembly. Only the high energetic electrons can pass the sample and reach the scintillator, causing an energy loss in the sensor like MIPs.
Figure 7.6 shows the results for the n-in-n and n-in-p sample, pointing out the depletion voltages. The sigma of the fit is the stated error. For the n-in-n sample the sensor is completely depleted at a bias voltage of about -20 V, whereas the n-in-p sample needs a bias voltage of -60 V. This is not due to the different types of bulk doping, but caused by the different doping concentrations of the two samples.
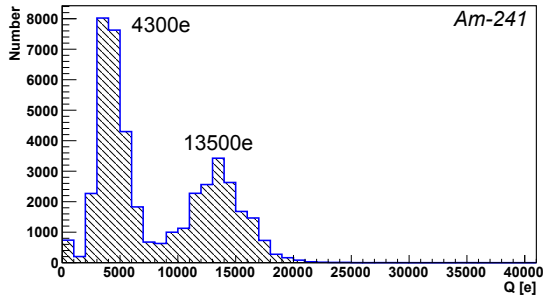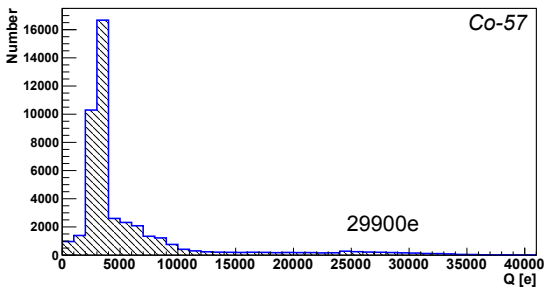
(a) Am-241 with SCC151.
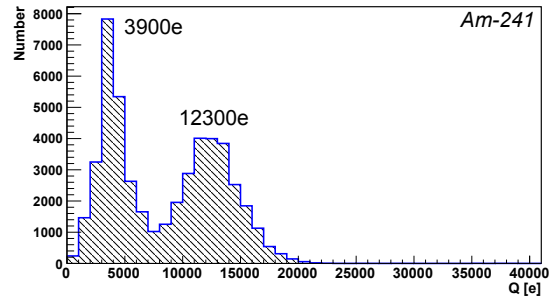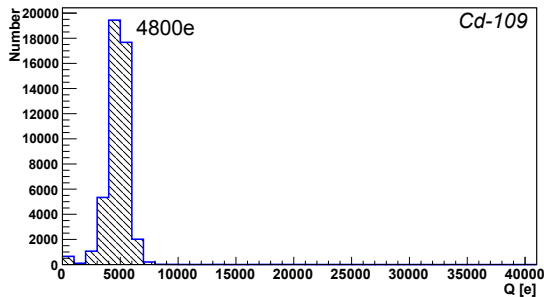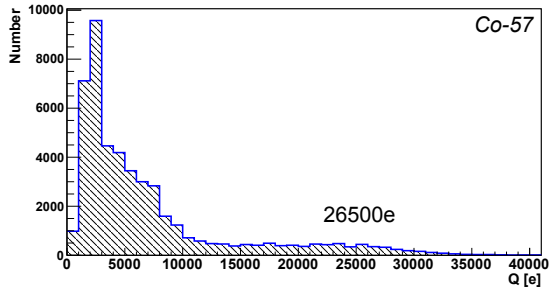
(b) Am-241 with SCC127.
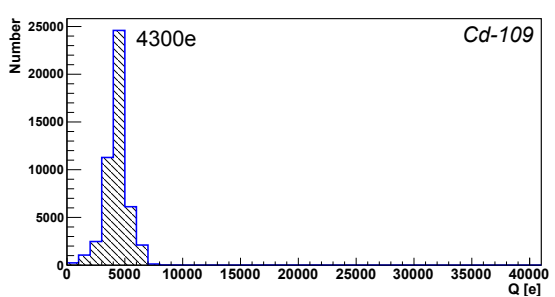
(c) Cd-109 with SCC151.

(d) Cd-109 with SCC127.

(e) Co-57 with SCC151.

(f) Co-57 with SCC127.

***Figure 7.5.:*** Spectra for Source Scans with americium 241, cadmium 109 and cobalt 57 for the n-in-n (SCC151) and n-in-p (SCC127) samples. The ToT is converted into charge using the ToT calibration described in Section 6.3 and the hits in neighbouring pixels are clustered.
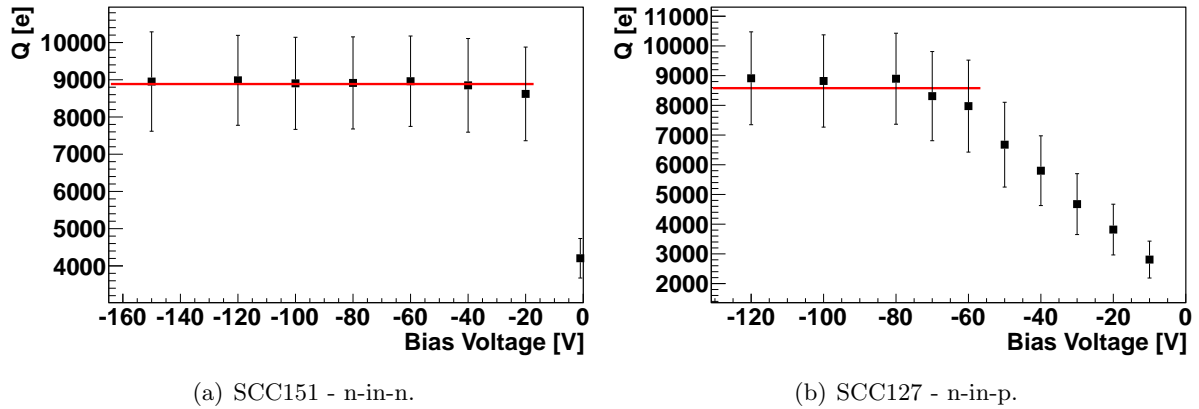
(a) SCC151 - n-in-n.

(b) SCC127 - n-in-p.

***Figure 7.6.:*** Results of several Source Scans versus sensor bias voltage with the unirradiated samples. The depletion voltage for the n-in-n (SCC151) sample is -20 V and for the n-in-p (SCC127) sample at -60 V.

## 7.2. Results of irradiated samples

The samples are irradiated in order to simulate the situation in ATLAS and future detectors. The radiation in a detector is caused by different particles, whereas for the irradiation for test reasons is only possible with protons or neutrons. The activity profile of the sensor depends on the type of irradiation.

In contrast to the unirradiated samples, the irradiated assemblies need to be cooled, not only during storage time, but as well while doing scans. A chiller cools down a cooling liquid to a temperature of $-60°$C, which is then pumped through a plate below the chip. The aluminium plate on which the front end is glued is connected via a copper strip to the cooling plate. This construction is surrounded by a 4 cm thick layer of expanded polystyrene, which has a thermal conductivity in the range from 0.032 W/mK to 0.038 W/mK, measured according to EN 12667. With this isolation it is possible to operate the chip at a temperature of $-35°$C.

Before any operations with the samples, problems with the wire bonds, which connect the sensor-chip assembly to the Single Chip Card, occurred. Before the samples are irradiated they have to be removed from the SCC and afterwards the wire bonds need to be set again. The second wire bond process has to be done more carefully, because the pads on the front end chip to which the wires are connected to, can contain rests of the old wires.
Both samples had to be rebonded before using. In addition, both SCCs showed short-circuits or loose connections that prevented operation. The n-in-p sample was connected to a new SCC before further testings and for the n-in-n sample the sensor bias voltage connection was exchanged.

### 7.2.1. IV Measurement

Due to the changed effective doping concentration the bias voltage to operate the samples has to be much higher compared to the unirradiated sensors. In Figure 7.7 the current-voltage characteristics of the irradiated n-in-n and n-in-p samples are shown. There is a difference of two orders of magnitude between the leakage currents of the two sensors. At a bias voltage of
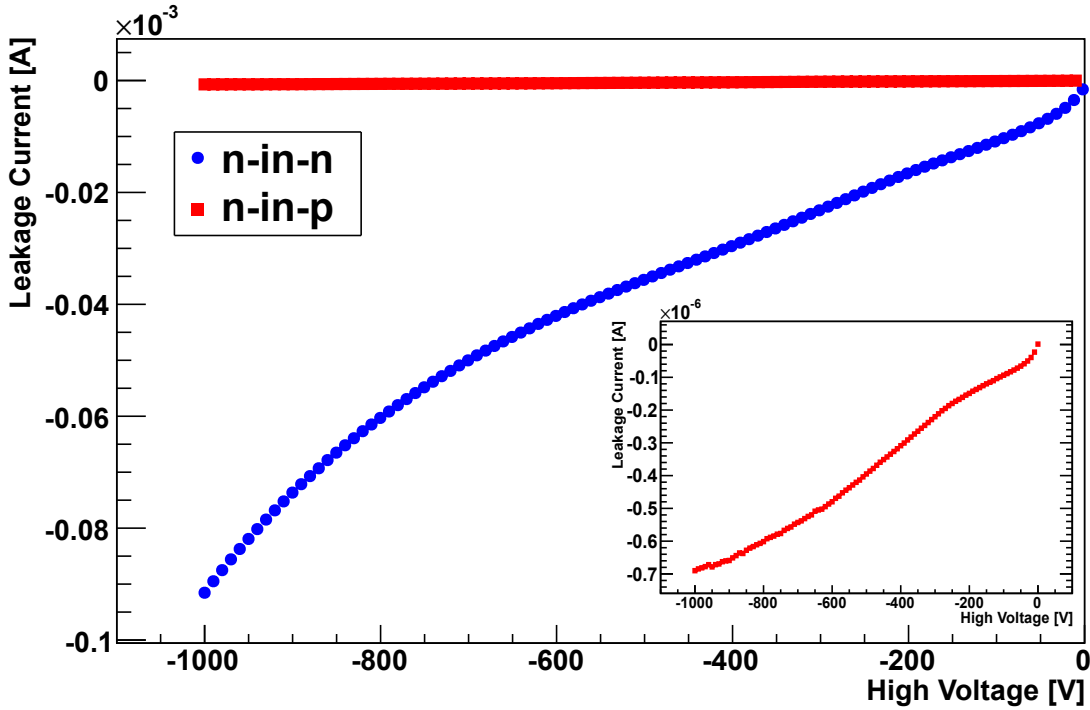
***Figure 7.7.:*** Current-voltage characteristic for irradiated n-in-n sample (PS4, blue) and n-in-p sample (SCC132, red). At a bias voltage of -1000 V the absolute value of the leakage current of the PS4 is hundred times larger than the one of the SCC132. The insert figure shows the characteristic of the n-in-p sample at a $10^{-6}$ A scale.

-1000 V the leakage current is about -90 $\mu$A for the n-in-n sample, whereas the n-in-p sample has only a current of -0.7 $\mu$A. Beside the absolute value, the shape of the two curves is similar, which can be seen in the small figure.

This n-in-p sample has no BCB insulation between sensor and front end chip, but nevertheless there is no sparking visible down to a voltage of -1000 V for either of the assemblies. Both samples are operated at a sensor bias voltage of -800 V, causing a leakage current of $-(60.30050 \pm 0.000001)$ $\mu$A for the n-in-n and $-(0.60146 \pm 0.00001)$ $\mu$A for the n-in-p sample.

### 7.2.2. Calibration and Tuning

An Analog Test shows some 1000 dead pixels for both sensors. This number can be reduced to less than 20 dead pixels by increasing the second stage feedback current `Amp2Vbpf` up to 80 DAC units.

To determine the `PlsrDAC` gradient $V_{\mathrm{Grad}}$ for both samples every eighth double-column is scanned (mode 2) starting with double-column 2 . The differences in the results are very small for varying starting columns and operation modes. The `PlsrDAC` offset determination is not straight forward due to problems with S-curve fitting. But the problems could be solved by increasing the $\chi^2$ cut value to 100,000 in order to get a reliable offset from the Injection Calibration Scan. Table 7.7 presents the resulting calibration parameters. 51$e$ for the n-in-n and 67$e$ for the n-in-p sample are injected per `PlsrDAC` step and the offset for the n-in-n and n-in-p sample is 730$e$ and 319$e$, respectively.

|  | $V_{\text{Grad}}$ | | | $V_{\text{offset}}$ | |
| --- | --- | --- | --- | --- | --- |
|  | [mV/DAC] | [e] | | [mV] | [e] |
| PS4 - n-in-n | 1.839 | 67 | | 20.1414 | 730 |
| SCC132 - n-in-p | 1.3970 | 51 | | 8,7895 | 319 |

***Table 7.7.:*** Resulting calibration parameters determined by DAC Scans for irradiated sensors with n-in-n (PS4) and n-in-p (SCC132) design.

After the `PlsrDAC` calibration, the discriminator threshold is tuned to $3000e$, $1600e$ and $800e$. The normal iterative tuning sequence of `TDAC` and `FDAC` tunings produces threshold distributions with large dispersions. Thus, each scan is checked and for example the chosen `GDAC` value is optimised. Furthermore, the number of steps of a fast `TDAC` tuning is increased until the `TDAC` distribution is in the middle of the range and the subsequent Threshold Scan produces sharp distributions and small dispersions. Moreover, the procedure of finding good values for `PrmpVbpf` and `FdacVbn` calculates negative values, which are impossible. Hence, very small values for the parameters are entered, causing unstable tuning results. But with a lot of intuition and patience the samples could be tuned to most of the intended thresholds and to a ToT of 10 bx at a charge of $15,000e$ (see Figure 7.8).
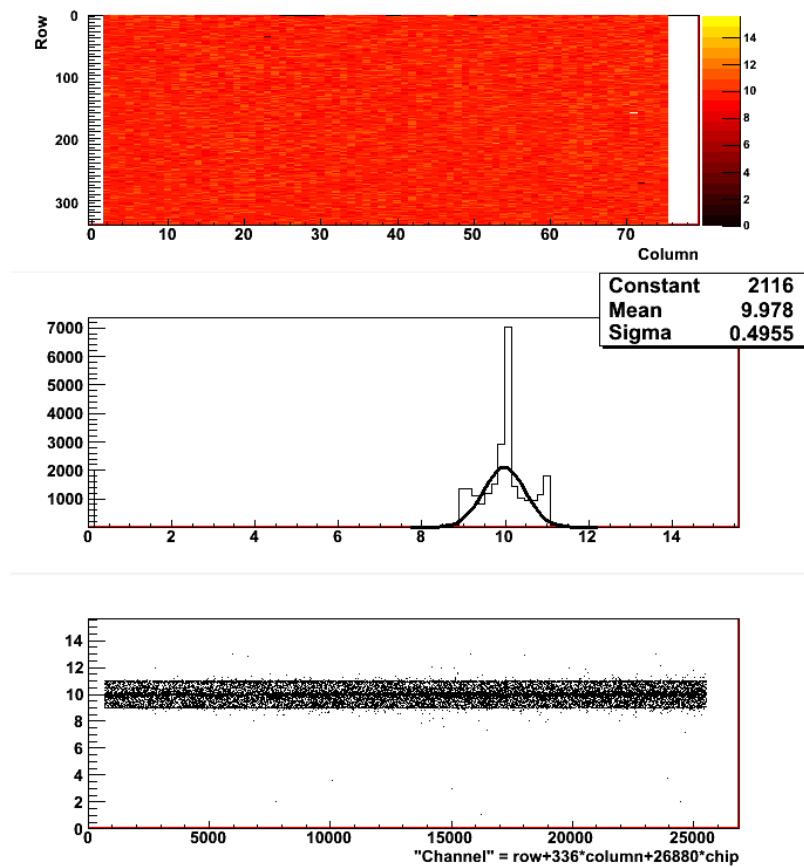


***Figure 7.8.:*** Resulting ToT spectrum of a `FDAC` tuning to 10 ToT at $15,000e$ with the irradiated n-in-p sample (SCC132).

### 7.2.3. Results of Threshold Scans

In Table 7.8 the results of the three Threshold Scans are presented, which are performed with sensor bias voltage. After the tuning sequence to a threshold of $1600e$, the resulting value for the n-in-n sample is $1700e$, which is accepted due to the reason of time. Thus, for the n-in-n sample all following results are for a threshold of $1700e$ instead of $1600e$.

For the irradiated samples different dispersion and noise values are observed for the different designs. The dispersion and the noise measured with the n-in-n sample decreases with the threshold, whereas these values are constant for the n-in-p sample and are comparable to the results of the unirradiated sensors. The higher noise for the n-in-n sensor is due to the much higher leakage current and the larger dispersion is caused by the more complicated tuning.

| PS4 - n-in-n | | | SCC132 - n-in-p | | |
|---|---|---|---|---|---|
| Threshold [e] | Dispersion [e] | Noise [e] | Threshold [e] | Dispersion [e] | Noise [e] |
| 3081 | 115 | 406 | 2998 | 27 | 178 |
| 1707 | 75 | 274 | 1611 | 26 | 133 |
| 791 | 56 | 208 | 799 | 35 | 170 |

***Table 7.8.:*** Discriminator threshold, dispersion and noise from Threshold Scans for the irradiated n-in-n (PS4) and n-in-p (SCC132) sample tuned to $3000e$, $1600e/1700e$ and $800e$.

The results of the Threshold Scan for $800e$ can be seen in Figure 7.9, showing similar results compared to the unirradiated samples. The noise for both sensor designs is about $20e$ higher than for the unirradiated samples, but the dispersion is in the same range between $30e$ and $60e$. There are between 500 and 1000 pixels in both samples that have a threshold below $400e$ and noise above $1000e$, indicating a failed S-curve fit. Thus, the threshold of $800e$ is close to the end of the dynamic range of the chip.

Furthermore, Threshold Scans without sensor bias voltage are performed and the results are shown in Table 7.9. Comparing the measurements with and without bias voltage, no differences can be seen. While the measurement of the lower thresholds is not possible for the unirradiated n-in-n sample, it is possible for the irradiated sample. This is due to the completed type inversion and the fact, that the $n^+$-type pixels are not short-circuited by the n-type bulk anymore.

| PS4 - n-in-n | | | SCC132 - n-in-p | | |
|---|---|---|---|---|---|
| Threshold [e] | Dispersion [e] | Noise [e] | Threshold [e] | Dispersion [e] | Noise [e] |
| 3079 | 108 | 387 | 2985 | 30 | 120 |
| 1706 | 77 | 268 | 1604 | 27 | 133 |
| 777 | 56 | 215 | 795 | 36 | 166 |

***Table 7.9.:*** Discriminator threshold, dispersion and noise from Threshold Scans without sensor bias voltage for the irradiated n-in-n (PS4) sample and the n-in-p (SCC132) sample tuned to $3000e$, $1600e/1700e$ and $800e$.
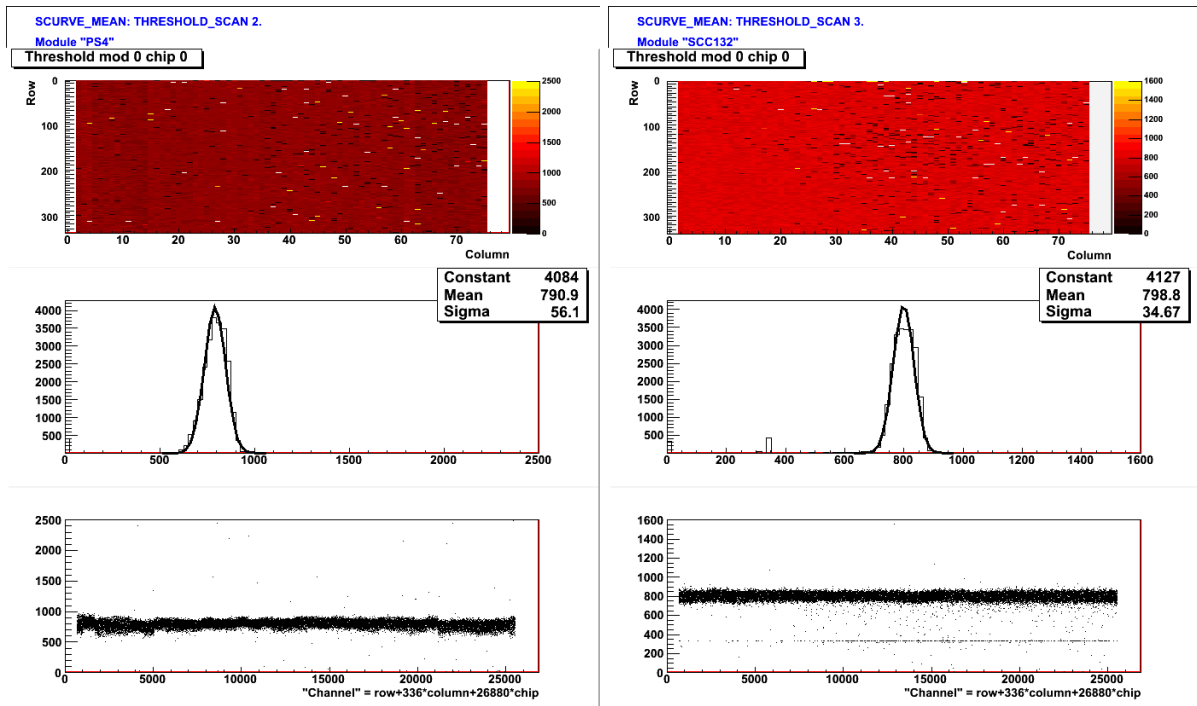
(a) Threshold for PS4.

(b) Threshold for SCC132.
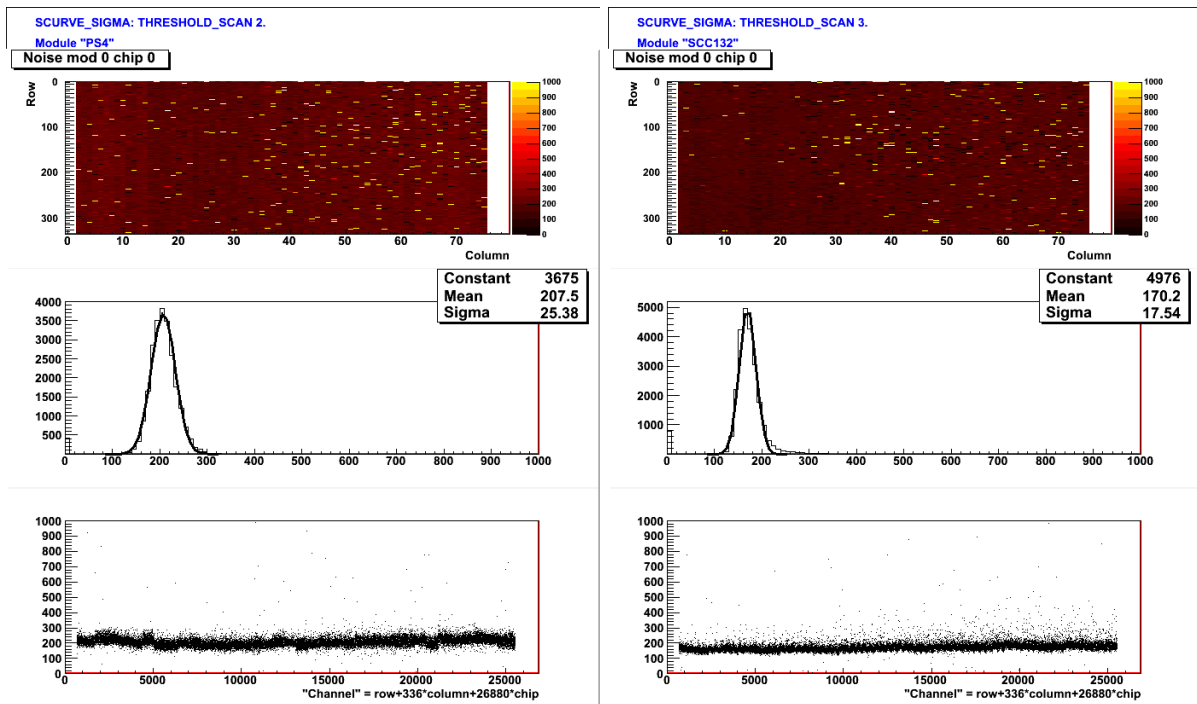


(c) Noise for PS4.

(d) Noise for SCC132.

***Figure 7.9.:*** Discriminator threshold (top) and noise (bottom) for a tuning target of $800e$ measured with the n-in-n sample (PS4, left) and the n-in-p sample (SCC132, right) showing no significant difference between the samples.

### 7.2.4. Crosstalk

The change in the effective doping concentration can be seen in the crosstalk as well. Before irradiation almost all pixels show crosstalk hits at a threshold of $800e$ and without bias voltage for both samples. Afterwards the number of pixels, which have a hit due to crosstalk is the same with and without sensor bias voltage. Hence, radiation damage changed the n-type bulk to p-type like bulk and the pixels are isolated.

Table 7.10 displays the number of hits for the different scenarios. The crosstalk increases with decreasing threshold, but even at a threshold of $800e$ only 6% to 11% of the pixels have a hit.

| Threshold | PS4 - n-in-n | | SCC132 - n-in-p | |
|---|---|---|---|---|
| | Number of pixels with crosstalk | | | |
| [e] | with HV | no HV | with HV | no HV |
| 3000 | 38 | 6 | 11 | 10 |
| 1600 | 70 | 45 | 66 | 58 |
| 800 | 1734 | 1756 | 2826 | 3043 |

***Table 7.10.:*** Number of pixels with hits due to crosstalk for the irradiated n-in-n (PS4) and n-in-p (SCC132) samples at thresholds tuned to $3000e$, $1600e/1700e$ and $800e$. Crosstalk Scans are performed with and without sensor bias voltage (HV).

### 7.2.5. Noise Occupancy

The results of the Noise Occupancy Scans are shown in Figure 7.10, showing the development of noise occupancy with changing threshold and sensor bias voltage. The data for the n-in-n sensor are indicated by blue dots and for the n-in-p sensor by red squares.

The mean noise occupancy per bunch crossing and pixel for different discriminator thresholds is shown in the top left plot. For a single Noise Occupancy Scan, $10^9$ triggers are sent. The development of the noise occupancy is similar for the two sensor designs, namely an increasing noise occupancy with decreasing threshold. The noise occupancy at a threshold of $3000e$ is one order of magnitude larger for the n-in-n sample, having a value of about $10^{-8}$, than for the n-in-p sample. If the threshold decreases, the difference between the two samples becomes smaller, down to a threshold of about $700e$, where both samples have about the same noise occupancy. The behaviour of the noise occupancy is supported by the number of masked pixels which increased as well for decreasing thresholds. The higher noise occupancy for the n-in-n sample is explained by the higher leakage current, making noise hits more likely.

In the top right plot the noise occupancy versus the sensor bias voltage is illustrated. For this measurement, $10^8$ triggers are sent. In contrast to the behaviour of the unirradiated samples, the bias voltage has no influence on the noise occupancy or the number of masked pixels. For the n-in-n sensor the noise occupancy is about $2 \cdot 10^{-8}$ and for the n-in-p sensor $3 - 4 \cdot 10^{-8}$. Both samples have about one per mill of all pixels masked.

### 7.2.6. Measurements with Radioactive Sources

For the n-in-n sensor, all Source Scans with the three different $\gamma$-sources produce the same spectrum, caused by the activity of the sensor itself. Next to the $\gamma$-transition of beryllium 7, positrons are produced by the $\beta^+$- transition of sodium 22. These low energy positrons create a

(a) Noise occupancy versus threshold.



(b) Noise occupancy versus bias voltage.



(c) Number of masked pixels versus threshold.



(d) Number of masked pixels versus bias voltage.
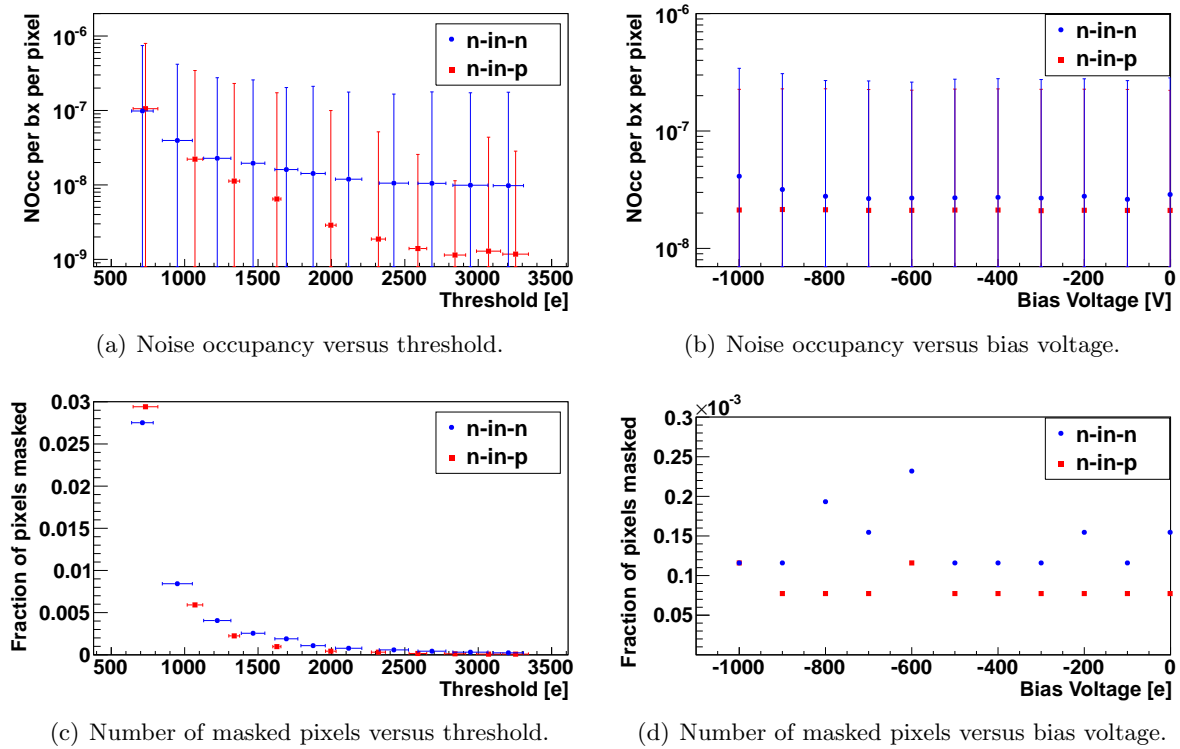
**Figure 7.10.:** Noise occupancy per bunch crossing (bx) and pixel (top) and number of masked pixels (bottom) versus Threshold (left) and sensor bias voltage (right) for the irradiated n-in-n (PS4, blue) and n-in-p (SCC132, red) sample.

lot of electron-hole pairs and the resulting ToT is large. This signal dominates all other signals and no other specific spectrum can be measured. But all measurements with the front end worked fine even with the high activity of the sensor. It is expected, that the sensor will still register hits from external particles using an external trigger source. The measurement with the scintillator as external trigger was not possible due to the temperature of $-35°C$, which is too cold for the photomultiplier.

With the n-in-n sample at least the spectrum of the sensor activation can be measured, in contrast to the irradiated n-in-p sample, which shows an behaviour that is not understood. For each external trigger the chip records hits for almost every pixel and thus no spectrum can be produced.

On top of the described problems, the concept of full depletion can not be used for a highly irradiated sensor, since the lifetime of a charge carrier is smaller than the time they are trapped by a defect centre.

# 8. Conclusion and Outlook

The performances of four thin sensors with two different sensor designs were characterised and compared before and after irradiation with regard to the HL-LHC requirements. A large radiation hardness and low production costs are needed for future large area tracking detectors. In the following the differences and similarities in the behaviour of the assemblies are described.

At first the differences in the results of the measurements are illustrated. The leakage current of the n-in-n sensors is larger compared to the n-in-p samples. Before irradiation, the leakage current of the n-in-n sample (SCC151) is about three times larger than the current of the n-in-p (SCC127). The difference increases to a more than 100 times larger leakage current after irradiation of the n-in-n sample (PS4) in contrast to the n-in-p sample (SCC132).
This result influences some other measurements. After irradiation, the noise of PS4 measured by a Threshold Scan is about two times larger than the noise of SCC132. This can also be seen in the noise occupancy, which is about one order of magnitude larger for PS4 than for SCC132.

The second large difference between the sensors with the differently doped bulk material is due to the development of the depletion zone. For an n-type bulk material the depleted region grows from the p-side to the pixel side. Thus, at low bias voltages the $n^+$ pixels are short-circuited via the n-type bulk.
This effect is observed in the results of the Threshold Scans without bias voltage. For thresholds of $1600e$ and $800e$ a threshold measurement for SCC151 is not possible, whereas SCC127 shows good results. In addition, without applied bias voltage the crosstalk for SCC151 is large compared to SCC127 as is the noise occupancy for low bias voltages.

Using Source Scans with a strontium 90 source at different bias voltages the depletion voltage of the unirradiated samples was determined. Due to different bulk doping concentrations the results are different. For SCC151 the depletion voltage is -20 V, whereas SCC127 is fully depleted at a voltage of -60 V.
For irradiated sensors the concept of full depletion is not used due to trapping caused by radiation damage.

Next to the differences between the two different sensor designs, there are differences due to the irradiation of the samples. It was found out that the tuning procedure to a certain threshold becomes harder if the chip is irradiated. The resulting dispersion is larger, but a Threshold Scan is still possible for all three thresholds.
Furthermore, the effects on the noise occupancy with varying bias voltage change. Before irradiation the noise occupancy increases with a lower absolute value of the bias voltage. Afterwards, the bias voltage has no influence on the noise occupancy.
A comparison of the results from the Source Scans before and after irradiation is not possible, because of the sensor activity of PS4 and the not understood behaviour of SCC132.

Subsequently, the similarities of the results obtained with the different samples are listed. The

tuning to the desired discriminator thresholds is possible for all of the four samples. Especially the tuning to $800e$ shows good results, which is important to measure reduced signals after radiation damage.

The shape of the $\gamma$-spectra of SCC151 and SCC127, which were obtained by Source Scans, is comparable. The conversion of the ToT values into charge is done with the ToT calibration for FE-I4, which was developed during the work of this thesis. The calibration was tested with different radioactive sources and charge injections. In order to explain the resulting discrepancy between the expected and measured charge two measurements were performed. The determination of the systematic errors of the calibration is still to be done.

After irradiation PS4 and SCC132 behave similarly during testing. There are no significant differences in the results of Threshold, Crosstalk and Noise Occupancy Scans.

Beside the different leakage current, which has an influence on the noise of the samples, no different behaviour of PS4 and SCC132 after irradiation is found. All measurements need to be repeated with a larger number of samples to remove effects by the low statistic.

The tested samples were irradiated with the expected fluence for IBL. In order to use the sensors for the HL-LHC the tests need to be repeated with a fluence of about $2 \cdot 10^{16}$ $n_{\mathrm{eq}}/\mathrm{cm}^2$. Furthermore, measurements with larger modules, like 4-chip modules, need to be done. If the reduced production costs of the single-sided processed n-in-p samples are confirmed, they are a good candidate for future upgrades.

# A. Additional Plots
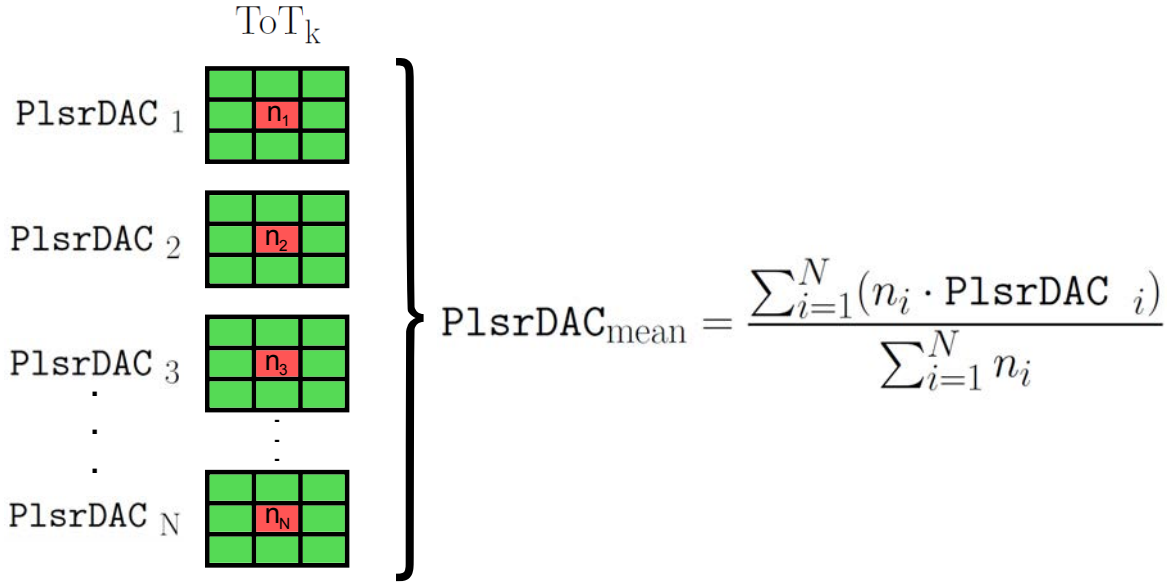


**Figure A.1.:** Presentation of the working sequence of the ToT Calibration Scan. For one ToT value $N$ pixel maps for different `PlsrDAC` values are produced. $n_i$ is the number that indicates how often this ToT is produced for the corresponding `PlsrDAC` $_i$. From theses numbers the $\text{PlsrDAC}_{\text{mean}}$ value is calculated.

(a) Crosstalk @ 3000$e$ for SCC151.

(b) Crosstalk @ 3000$e$ for SCC127.

(c) Crosstalk @ 1600$e$ for SCC151.

(d) Crosstalk @ 1600$e$ for SCC127.

(e) Crosstalk @ 800$e$ for SCC151.

(f) Crosstalk @ 800$e$ for SCC127.
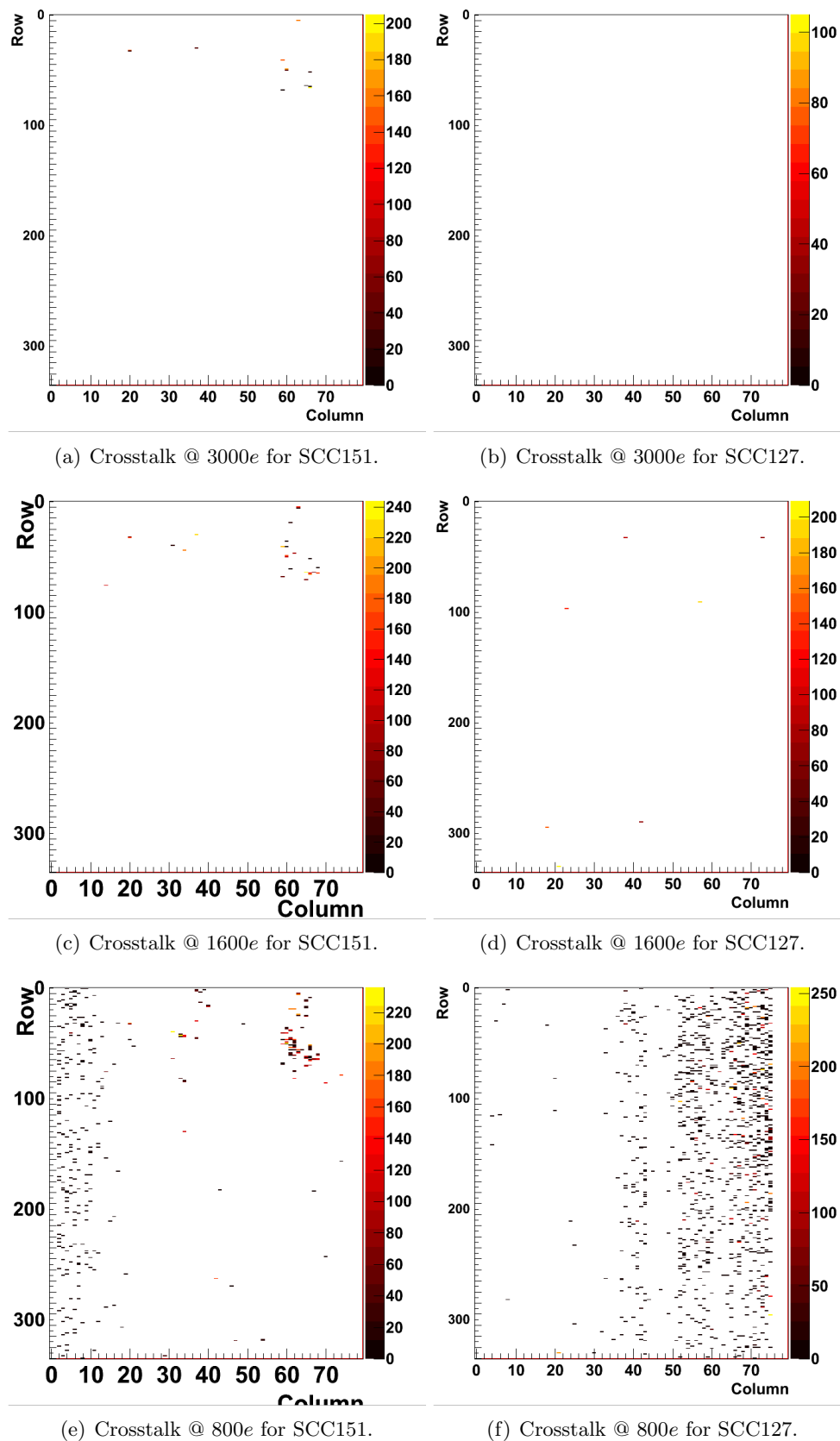
***Figure A.2.:*** Results for several Crosstalk Scans for a threshold tuned to 3000$e$ (top), 1600$e$ (middle) and 800$e$ (bottom) for the unirradiated n-in-n (SCC151, left) and n-in-p (SCC127, right) samples, measured **with** sensor bias voltage.
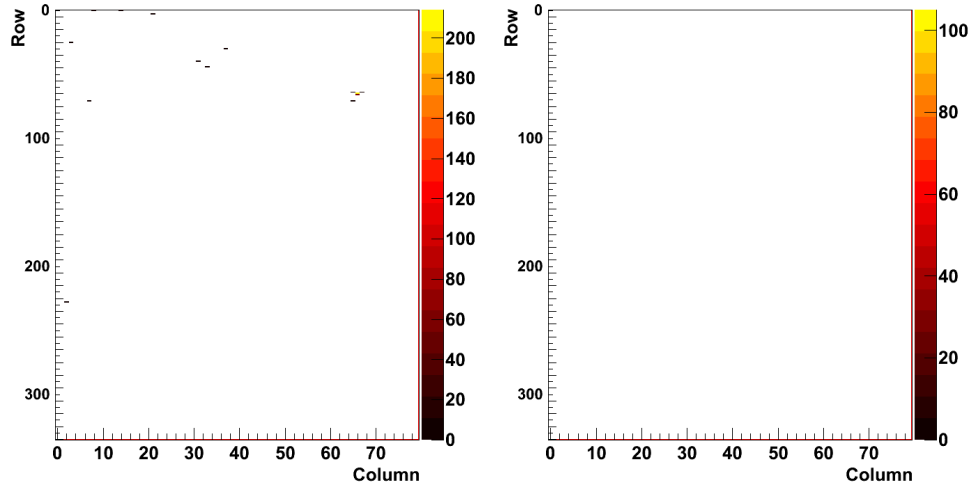
(a) Crosstalk @ 3000e for SCC151.
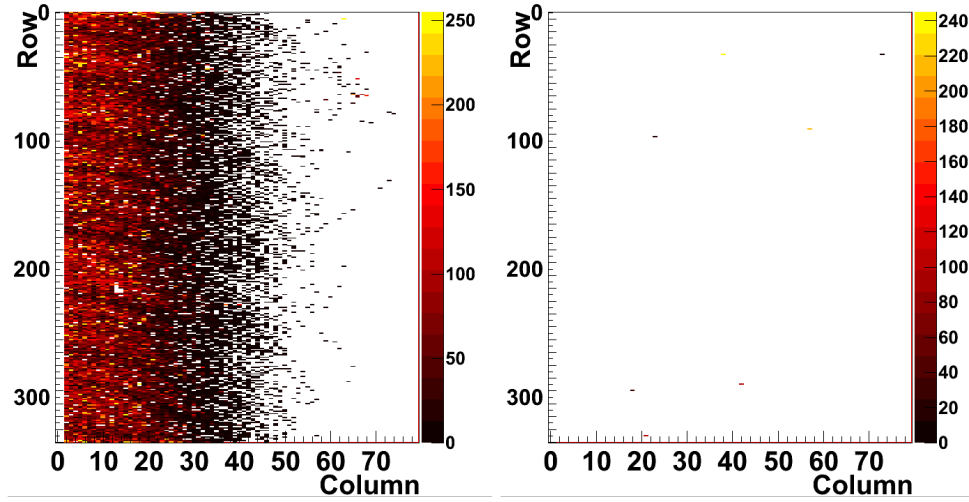
(b) Crosstalk @ 3000e for SCC127.

(c) Crosstalk @ 1600e for SCC151.

(d) Crosstalk @ 1600e for SCC127.
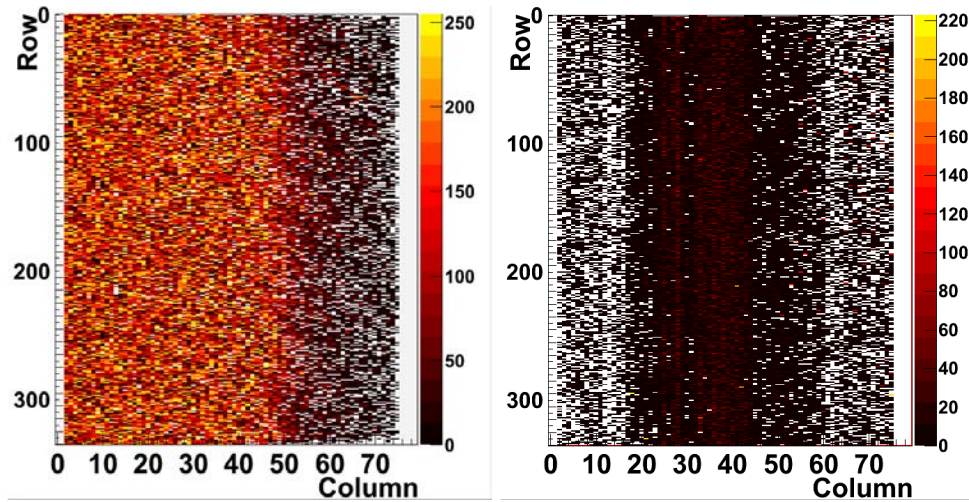
(e) Crosstalk @ 800e for SCC151.

(f) Crosstalk @ 800e for SCC127.

**Figure A.3.:** Results for several Crosstalk Scans for a threshold tuned to 3000e (top), 1600e (middle) and 800e (bottom) for the unirradiated n-in-n (SCC151, left) and n-in-p (SCC127, right) samples, measured **without** sensor bias voltage.
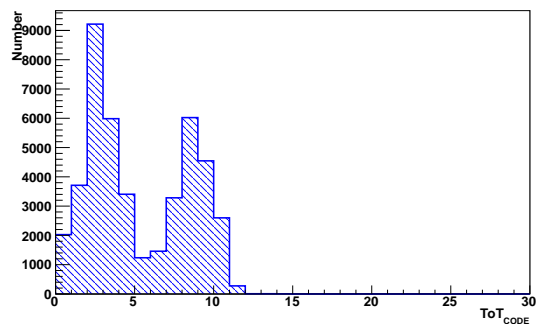
(a) Am-241 with SCC151.
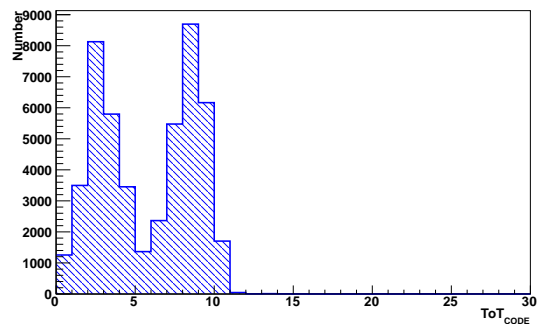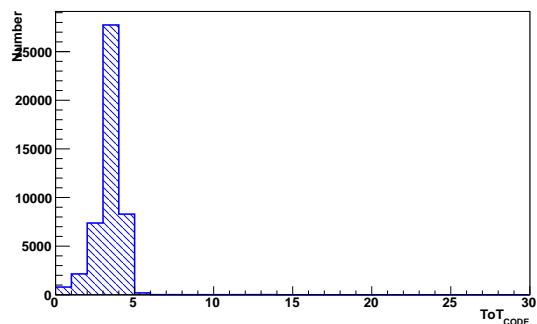
(b) Am-241 with SCC127.
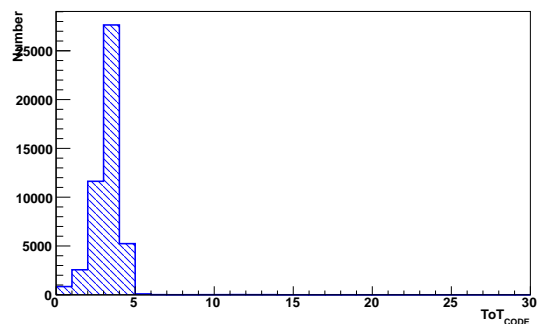
(c) Cd-109 with SCC151.

(d) Cd-109 with SCC127.
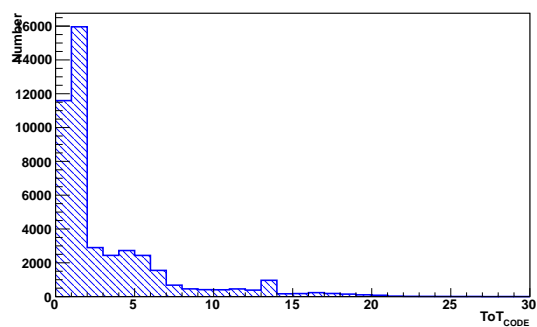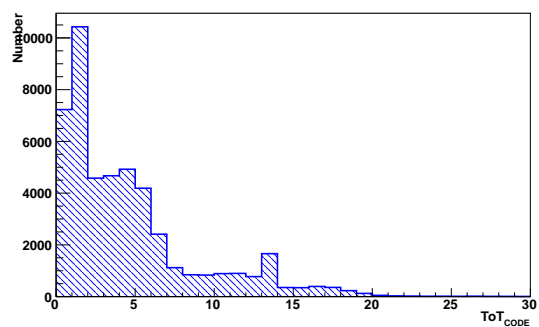
(e) Co-57 with SCC151.

(f) Co-57 with SCC12.

***Figure A.4.:*** ToT$_{Code}$-Spectra for Source Scans with americium 241, cadmium 109 and cobalt 57 for the n-in-n (SCC151) and n-in-p (SCC127) samples. The ToT is tuned to 10 ToT @ 15,000$e$ and the hits in neighbouring pixels are clustered.

# B. List of Digital Analogue Converters (DAC)

| DAC | Control | Size |
|-----|---------|------|
| Amp2Vbpf | Second Stage Feedback Current | 8-bit |
| Colpr_Addr | Address of Double-Column for all Double-Column Operations | 6-bit |
| Colpr_Mode | Affected Double-Columns Relative to Addressed Colpr_Addr | 2-bit |
| FDAC | In-Pixel Preamplifier Feedback Current | 4-bit |
| FdacVbn | Step Size for In-pixel Preamplifier Feedback Current | 8-bit |
| PlsrDAC | Calibration Injection Voltage Value (former VCAL) | 10-bit |
| PrmpVbpf | Global Preamplifier Feedback Current | 8-bit |
| TDAC | In-Pixel Discriminator Threshold Input | 5-bit |
| Vthin_Alt (GDAC) | Global Discriminator Threshold Input (Temperature Compensated; Coarse and Fine Adjustment) | 16-bit |

# Bibliography

[1] D. Griffiths, *Introduction to Elementary Particles*. Physics Textbook. John Wiley & Sons, 2008.

[2] *CERN Summer Student Webfest 2012*, `http://www.citizencyberscience.net/wiki/index.php?title=Standard_Model,_Standard_Infographic`. website, visited on August 22th, 2012.

[3] P. W. Higgs, *Broken Symmetries and the Masses of Gauge Bosons*, Phys. Rev. Lett. **13** (Oct, 1964) 508–509.

[4] F. Englert and R. Brout, *Broken Symmetry and the Mass of Gauge Vector Mesons*, Phys. Rev. Lett. **13** (Aug, 1964) 321–323.

[5] G. S. Guralnik, C. R. Hagen, and T. W. B. Kibble, *Global Conservation Laws and Massless Particles*, Phys. Rev. Lett. **13** (Nov, 1964) 585–587.

[6] ATLAS Collaboration, Aad et al., *Observation of a new particle in the search for the Standard Model Higgs boson with the ATLAS detector at the LHC*, Physics Letters B **716** (2012) no. 1, 1 – 29.

[7] CMS Collaboration, Chatrchyan et al., *Observation of a new boson at a mass of 125 GeV with the CMS experiment at the LHC*, Physics Letters B **716** (2012) no. 1, 30 – 61.

[8] O. Boyarkin, *Advanced Particle Physics Volume 2: The Standard Model and Beyond*. Advanced Particle Physics. Taylor & Francis, 2010.

[9] D. J. Fixsen, *The Temperature of the Cosmic Microwave Background*, The Astrophysical Journal **707** (2009) no. 2, 916.

[10] O. S. Brüning et al., *LHC Design Report*. CERN, Geneva, 2004.

[11] G. Kane and A. Pierce, *Perspectives on LHC Physics*. World Scientific, 2008.

[12] ATLAS Collaboration, *Luminosity Public Results*, `https://twiki.cern.ch/twiki/bin/view/AtlasPublic/LuminosityPublicResults`. website, visited on August 20th, 2012.

[13] ATLAS Collaboration, G. Aad et al., *The ATLAS Experiment at the CERN Large Hadron Collider*, JINST **3** (2008) S08003.

[14] ATLAS Collaboration, *ATLAS Detector and Physics Performance Technical Design Report*, Tech. Rep. CERN-LHCC-99-014 and CERN-LHCC-99-015, CERN, Geneva, 1999.

[15] ATLAS Collaboration, C. Padilla et al., *The ATLAS Trigger System*, IEEE Trans. Nucl. Sci. **57** (Apr, 2010) 650–657.

[16] ATLAS Collaboration, *ATLAS Inner Detector Technical Design Report*, Tech. Rep. CERN-LHCC-97-016 and CERN-LHCC-97-017, CERN, Geneva, 1997.

[17] ATLAS Collaboration, *ATLAS Calorimeter Performance Technical Design Report*, Tech. Rep. CERN-LHCC-96-040, CERN, Geneva, 1997.

[18] ATLAS Collaboration, *ATLAS Muon Spectrometer Technical Design Report*, Tech. Rep. CERN-LHCC-97-022, CERN, Geneva, 1997.

[19] M. Capeans et al., *ATLAS Insertable B-Layer Technical Design Report*, Tech. Rep. CERN-LHCC-2010-013, CERN, Geneva, Sep, 2010.

[20] M. Barbero et al., *The FE-I4 pixel readout chip and the IBL module*, PoS **VERTEX2011** 038.

[21] G. Aad et al., *ATLAS pixel detector electronics and sensors*, JINST **3** (2008) P07007.

[22] W. Leo, *Techniques for nuclear and particle physics experiments: a how-to approach.* Springer, 1994.

[23] C. Grupen, *Teilchendetektoren.* BI-Wissenschaftsverlag, 1993.

[24] K. Nakamura et al., *Review of Particle Physics*, J. Phys. G **37** (2010) 075021. Particle Data Group.

[25] Collaboration Authors and A Editors of the LB Volumes III/17A-22A-41A1b, *Landolt-Börnstein - Group III Condensed Matter: Numerical Data and Functional Relationships in Science and Technology*, vol. 41A1b: Group IV Elements, IV-IV and III-V Compounds. Part b - Electronic, Transport, Optical and Other Properties, ch. Silicon (Si), intrinsic carrier concentration. Springer, 2012.

[26] M. Beimforde, *Development of thin sensors and a novel interconnection technology for the upgrade of the ATLAS pixel system.* PhD thesis, TU München, 2010.

[27] V. A. J. Van Lint, *Mechanisms of radiation effects in electronic materials.* Wiley, New York, 1980.

[28] J. Srour, C. Marshall, and P. Marshall, *Review of displacement damage effects in silicon devices*, IEEE Trans. Nucl. Sci. **50** (Jun, 2003) 653 – 670.

[29] R. Wunstorf, *Systematische Untersuchungen zur Strahlenresistenz von Silizium-Detektoren für die Verwendung in Hochenergiephysik-Experimenten.* PhD thesis, Universität Hamburg, DESY, Oct, 1992.

[30] J. R. Srour and R. A. Hartmann, *Enhanced displacement damage effectiveness in irradiated silicon devices*, IEEE Trans. Nucl. Sci. **36** (Dec, 1989) 1825 – 1830.

[31] M. Moll, *Radiation Damage in Silicon Particle Detectors.* PhD thesis, Universität Hamburg, Nov, 1999.

[32] T. Rohe, *Design and test of pixel sensors for the ATLAS pixel detector*, Nucl. Instr. and Meth. A **460** (2001) 55 – 66.

[33] ATLAS IBL Collaboration, *Prototype ATLAS IBL Modules using the FE-I4A Front-End Readout Chip*, ArXiv e-prints (Sep, 2012) , `arXiv:1209.1906`.

[34] A. Macchiolo et al., *Performance of n-in-p pixel detectors irradiated at fluences up to $5 \times 10^{15} \ n_{eq}/cm^2$ for the future ATLAS upgrades*, ArXiv e-prints (Oct, 2011) , `arXiv:1110.4468`.

[35] P. Weigell et al., *Characterization and Testbeam Analysis of irradiated Silicon n-in-p Pixel Detectors for the ATLAS Upgrades*, 18th RD50 Workshop Liverpool, May, 2011.

[36] G. Casse et al., *Enhanced efficiency of segmented silicon detectors of different thicknesses after proton irradiations up to $1 \times 10^{16} \ n_{eq}/cm^2$*, Nucl. Inst. and Meth. A **624** (2010) 401 – 404.

[37] L. Andricek et al., *Processing of ultra thin silicon sensors for future e+e- linear collider experiments*, in *IEEE Nuclear Science Symposium Conference Record*, vol. 3, pp. 1655 – 1658. Oct, 2003.

[38] R. Wunstorf, *Radiation tolerant sensors for the ATLAS pixel detector*, Nucl. Instr. and Meth. A **466** (2001) 327 – 334.

[39] C. Da Viá et al., *3D active edge silicon sensors with different electrode configurations: Radiation hardness and noise performance*, Nucl. Inst. and Meth. A **604** (2009) 505 – 511.

[40] P. Hansson et al., *3D silicon pixel sensors: Recent test beam results*, Nucl. Inst. and Meth. A **628** (2011) 216 – 220.

[41] R. S. Wallny, *Status of diamond detectors and their high energy physics application*, Nucl. Inst. and Meth. A **582** (2007) 824 – 828.

[42] D. Asner et al., *Diamond pixel modules*, Nucl. Inst. and Meth. A **636** (2011) 125 – 129.

[43] *USBpix - USB based readout system for ATLAS FE-I3 and FE-I4*, `http://icwiki.physik.uni-bonn.de/twiki/bin/view/Systems/UsbPix`. website, visited on September 8th, 2012.

[44] M. Backhaus et al., *Development of a versatile and modular test system for ATLAS hybrid pixel detectors*, Nucl. Inst. and Meth. A **650** (2011) no. 1, 37 – 40.

[45] *PixLib Scans*, `http://icwiki.physik.uni-bonn.de/twiki/bin/view/Systems/PixLibScans`. website, visited on September 11th, 2012.

[46] FE-I4 Collaboration, *The FE-I4A Integrated Circuit Guide*, Version 11.1, Unpublished Internal Note, Feb, 2011.

[47] M. Donzelli, *Studies of in-time charge measurement with the read-out chip of the first upgrade stage of the ATLAS Pixel Detector*. Georg-August-Universität Göttingen. Feb, 2012. Bachelor's Thesis.

[48] Laboratoire National Henri Becquerel, *Online database of radionuclide decay data*, `http://www.nucleide.org/DDEP_WG/DDEPdata.htm`. website, visited on February 13th, 2012.

# List of Figures

# List of Tables

# Danksagung

Zunächst möchte ich mich bei all denjenigen bedanken, die mich während der Anfertigung dieser Masterarbeit unterstützt und motiviert haben.

Mein ganz besonderer Dank gilt meinen Eltern, die mich immer unterstützen, mir den Rücken freihalten und ein offenes Ohr für all meine Probleme haben. Und natürlich Alexander, der immer für mich da ist und mir mit Rat und Tat zu Seite steht.

Ich danke Prof. Dr. Arnulf Quadt für das Angebot diese Arbeit im II. Physikalischen Institut zu schreiben und dafür, dass er sich bereit erklärt hat mein Zweitgutachter zu sein.
Des Weiteren danke ich PD Dr. Jörn Große-Knetter für die Betreuung meiner Arbeit und die gute Aufnahme in das Hardware-Team. Ich konnte immer zu ihm kommen und Fragen stellen, die mir freundlich und fachlich beantwortet wurden.

Ein ganz besonderer Dank gilt auch Dr. Jens Weingarten für die Betreuung, die viele hilfreiche Vorschläge und guten Ratschläge. Vielen Dank für die Geduld und Mühen.
Danke auch an Jens und Matze für das geduldige Korrekturlesen meiner Arbeit.

Natürlich ein großer Dank an alle Leute der Hardware für die Hilfe und die Bereitschaft meine Fragen zu beantworten. Andre, Hans, Jens, Johannes, Jörn, Lars, Markus, Mattia, Matze und Nina, ohne euch wäre die Arbeit lange nicht so lustig und schön gewesen.
Furthermore, I would like to thank all the members of the II. Institute of Physics for the enjoyable and friendly atmosphere and the very good time I had. Especially, I would like to thank my office mates for the wonderful distractions.

Nicht zu vergessen ist die große Hilfe der beiden Werkstätten für die schnelle und gute Anfertigung von Haltern, Kabeln und sonstigen Teilen und dem Sekretariat für die Bewältigung des Papierkrams. DANKE.

Zu guter Letzt danke ich meiner Göttinger Truppe für die vielen schönen Aktivitäten, die Unterstützung und aufbauenden Worte, wenn mal wieder etwas nicht funktioniert hat.

**Erklärung**  nach §18(8) der Prüfungsordnung für den Bachelor-Studiengang Physik und den Master-Studiengang Physik an der Universität Göttingen:

Hiermit erkläre ich, dass ich diese Abschlussarbeit selbständig verfasst habe, keine anderen als die angegebenen Quellen und Hilfsmittel benutzt habe und alle Stellen, die wörtlich oder sinngemäß aus veröffentlichten Schriften entnommen wurden, als solche kenntlich gemacht habe.

Darüberhinaus erkläre ich, dass diese Abschlussarbeit nicht, auch nichtauszugsweise, im Rahmen einer nichtbestandenen Prüfung an dieser oder einer anderen Hochschule eingereicht wurde.

Göttingen, den 28.09.2012

(Julia Rieger)